



**Room temperature charge density wave in a tetragonal polymorph of  $Gd_2Os_3Si_5$  and study of its origin in the  $RE_2T_3X_5$  ( $RE =$  Rare earth,  $T =$  transition metal,  $X =$  Si, Ge) series**

Vikash Sharma,<sup>\*,†</sup> Sitaram Ramakrishnan,<sup>\*,‡,¶</sup> S. S. Jayakrishnan,<sup>§</sup> Surya Rohith Kotla,<sup>||</sup> Bishal Maiti,<sup>†</sup> Claudio Eisele,<sup>||</sup> Harshit Agarwal,<sup>||</sup> Leila Noohinejad,<sup>⊥</sup> M. Tolkiehn,<sup>⊥</sup> Dipanshu Bansal,<sup>\*,§</sup> Sander van Smaalen,<sup>\*,||</sup> and Arumugam Thamizhavel<sup>\*,†</sup>

<sup>†</sup>*Department of Condensed Matter Physics and Materials Science, Tata Institute of Fundamental Research, Mumbai 400005, India*

<sup>‡</sup>*Department of Quantum Matter, AdSE, Hiroshima University, Higashi-Hiroshima 739-8530, Japan*

<sup>¶</sup>*I-HUB Quantum Technology Foundation, Indian Institute of Science Education and Research, Pune 411008, India*

<sup>§</sup>*Department of Mechanical Engineering, Indian Institute of Technology Bombay, Mumbai, MH 400076, India*

<sup>||</sup>*Laboratory of Crystallography, University of Bayreuth, 95447 Bayreuth, Germany*

<sup>⊥</sup>*P24, PETRA III, Deutsches Elektronen-Synchrotron DESY, Notkestrasse 85, 22607 Hamburg, Germany*

E-mail: vikash.sharma@tifr.res.in; niranj002@gmail.com; dipanshu@iitb.ac.in;  
smash@uni-bayreuth.de; thamizh@tifr.res.in

**Abstract**

Charge density wave (CDW) systems are proposed to exhibit application potential for electronic and optoelectronic devices. However, CDWs often develop at cryogenic temperatures, which hinders their applications. Therefore, identifying new materials that exhibit a CDW state at room temperature is crucial for the development of CDW-based devices. Here, we present a non-layered tetragonal polymorph of  $\text{Gd}_2\text{Os}_3\text{Si}_5$ , which exhibits a CDW state at room temperature.  $\text{Gd}_2\text{Os}_3\text{Si}_5$  assumes the tetragonal  $\text{Sc}_2\text{Fe}_3\text{Si}_5$  structure type with the space group  $P4/mnc$ . Single-crystal X-ray diffraction (SXRD) analysis shows that  $\text{Gd}_2\text{Os}_3\text{Si}_5$  possesses an incommensurately modulated structure with modulation wave vector  $\mathbf{q} = (0.53, 0, 0)$ , while the modulation reduces the symmetry to orthorhombic  $Cccm(\sigma 00)0s0$ . This differs from isostructural  $\text{Sm}_2\text{Ru}_3\text{Ge}_5$ , where the modulated phase has been reported to possess monoclinic symmetry  $Pm(\alpha 0 \gamma)0$ . Reinvestigation of  $\text{Sm}_2\text{Ru}_3\text{Ge}_5$  suggests that its modulated crystal structure can alternatively be described by  $Cccm(\sigma 00)0s0$ , with modulations similar to  $\text{Gd}_2\text{Os}_3\text{Si}_5$ . The temperature-dependent magnetic susceptibility indicates an antiferromagnetic transition at  $T_N \approx 5.5$  K. Furthermore it shows an anomaly at around 345 K, suggesting a CDW transition at  $T_{\text{CDW}} = 345$  K, in agreement with high-temperature SXRD measurements. The temperature-dependent electrical resistivity has a maximum at a lower temperature, that we nevertheless identify with the CDW transition, and that can be described as an insulator-to-metal transition (IMT). The calculated electronic band structure indicates q-dependent electron-phonon coupling as dominant mechanism of CDW formation in tetragonal  $\text{Gd}_2\text{Os}_3\text{Si}_5$ . The modulated structure then indicates a major involvement of the Si2a atom in the CDW modulations. Compounds  $RE_2T_3X_5$  ( $RE =$  rare earth,  $T =$  transition metal,  $X =$  Si, Ge) have been reported with either the tetragonal  $\text{Sc}_2\text{Fe}_3\text{Si}_5$  structure type or the orthorhombic  $\text{U}_2\text{Co}_3\text{Si}_5$  structure type. Not all of these compounds undergo CDW phase transitions. We find that  $RE_2T_3X_5$  compounds will exhibit a CDW transition, if the condition  $0.526 < c/\sqrt{ab} < 0.543$  is satisfied.

# Introduction

A charge-density-wave (CDW) is a modulation of the electronic density of a metallic, crystalline material, which is accompanied by a periodic lattice distortion (PLD) of the atomic positions.<sup>1-7</sup> The wavelength of the CDW/PLD represents an independent period in the system, such that, in general, the material becomes an aperiodic crystal. A CDW can develop upon cooling a sample from the normal state,<sup>3,7</sup> or by applying pressure on it.<sup>8</sup> In the CDW phase, the electronic structure of a metallic system becomes modified. A gap opens up in the electronic density of states, which is often reflected in the physical properties, such as the electrical resistivity and magnetic susceptibility, and in spectroscopic experiments.<sup>3,4,7,9,10</sup> There are various techniques to probe the CDW state, such as X-ray diffraction (XRD),<sup>10,11</sup> scanning tunnelling microscopy (STM),<sup>4,12</sup> transmission electron microscopy (TEM),<sup>13</sup> angle resolved X-ray photoelectron spectroscopy (ARPES),<sup>4</sup> nuclear magnetic resonance (NMR),<sup>14</sup> Raman spectroscopy<sup>15</sup> and ultrafast pump-probe experiments.<sup>16</sup> A metal-to-insulator transition (MIT), obvious in the electrical resistivity, together with the appearance of superlattice reflections in XRD are the typical characteristic features pointing toward a CDW state.<sup>6,7,17-19</sup>

Compounds  $RE_2T_3X_5$  ( $RE$  = Rare earth,  $T$  = transition metal,  $X$  = Si, Ge) are known to exhibit polymorphism, crystallizing in either the  $Sc_2Fe_3Si_5$  structure type with the tetragonal space group  $P4/mnc$  or the  $U_2Co_3Si_5$  structure type with the orthorhombic space group  $Ibam$ .<sup>20</sup> CDW transitions have been observed for compounds with either structure type. For example, Ramakrishnan *et al.*<sup>17-19</sup> reported CDW transitions in three orthorhombic compounds  $RE_2Ir_3Si_5$ , with transition temperatures  $T_{CDW} = 90$  K for  $RE = Ho$ ,  $T_{CDW} = 150$  K for  $RE = Er$ , and  $T_{CDW} = 200$  K for  $RE = Lu$ . Moreover,  $Ho_2Ir_3Si_5$  shows coupling between CDW ordering and magnetism.<sup>17</sup> XRD studies pointed towards zigzag chains of Ir atoms being responsible for the stabilization of the CDW in these compounds.<sup>17-19</sup> Bugaris *et al.*<sup>7</sup> have reported CDW transitions in the tetragonal compounds  $RE_2Ru_3Ge_5$  ( $RE = Pr, Sm, Dy$ ), with  $T_{CDW} = 200$  K for  $RE = Pr$ , and  $T_{CDW} = 175$  K for  $RE = Sm$ . Stabilization

of the CDWs was attributed to a PLD on the zigzag chains of Ge.<sup>7</sup> Interestingly, one such compound  $\text{Sm}_2\text{Ru}_3\text{Ge}_5$  shows CDW transitions in both the orthorhombic and tetragonal polymorphs.<sup>7,21,22</sup>

There are other compounds in the series  $RE_2T_3X_5$  that do not exhibit CDW transitions, despite being isostructural to the orthorhombic or tetragonal structure types. For example, orthorhombic compounds  $RE_2\text{Ir}_3\text{Si}_5$  containing lighter rare-earth elements  $RE = \text{La}, \text{Ce}$  or  $\text{Gd}$ , do not show CDW transitions.<sup>23</sup> Tetragonal compounds  $RE_2\text{Ru}_3\text{Ge}_5$  do not exhibit CDW order for rare-earth elements  $RE$  other than those mentioned above.<sup>7</sup> Furthermore, tetragonal compounds  $RE_2\text{Re}_3\text{Si}_5$  ( $RE = \text{Ce}, \text{Pr}, \text{Ho}$ ) do not exhibit CDW transitions in the temperature range 2 – 300 K.<sup>24,25</sup>

In one of the earlier studies,  $\text{Gd}_2\text{Os}_3\text{Si}_5$  has been reported with the orthorhombic  $\text{U}_2\text{Co}_3\text{Si}_5$  structure type, albeit with disorderly occupation of one of the two Os sites by Os/Si, resulting in the composition  $\text{Gd}_2\text{Os}_{2.82(2)}\text{Si}_{5.14(2)}$ .<sup>26</sup> However, no physical properties have been reported so far. Here, we report the synthesis and characterization of a new polymorph of  $\text{Gd}_2\text{Os}_3\text{Si}_5$ . It crystallizes in the tetragonal  $\text{Sc}_2\text{Fe}_3\text{Si}_5$  structure type with space group  $P4/mnc$ . We have discovered an incommensurate CDW state in this compound, which is characterized by the modulation wave vector  $\mathbf{q} = (0.53, 0, 0)$ . The onset of the CDW transition appears to be somewhere between 400 to 345 K, and thus shows the potential for applications in electronic devices.<sup>5,9,27–30</sup> Analysis by SXRD reveals that the CDW modulation is of orthorhombic symmetry with superspace group  $Cccm(\sigma 00)0s0$ , while the average crystal structure remains tetragonal. Using electronic structure calculations, we evaluated several mechanisms of CDW formation, including Fermi surface nesting and hidden nesting, and find that the wave vector-dependent electron-phonon coupling possibly controls the CDW formation. The electrical resistivity  $\rho(T)$  depicts an insulator to metal transition (IMT) at around 250 K along with a hysteresis during cooling and warming cycles in insulating as well as metallic regimes. This insulating behaviour is in line with observed weak superlattice reflections in SXRD at 300 K, pointing a CDW state even at room temperature. The magnetic susceptibility

$\chi(T)$  reveals an antiferromagnetic ordering at  $T_N \sim 5.5$  K, and in the paramagnetic state it exhibits hysteresis where the CDW transition is observed. The previous results of  $RE_2T_3X_5$  compounds have revealed that the dimensionality plays a key role in the formation of the CDW phase.<sup>7,17-19,23-25</sup> A criterion is proposed, which is based on the lattice parameters according to the value of  $c/\sqrt{ab}$ , where  $a$ ,  $b$  and  $c$  are the lattice parameters of the tetragonal or orthorhombic structure. We found that  $0.526 < c/\sqrt{ab} < 0.543$  needs to be fulfilled for the existence of a CDW state in a compound of the series of  $RE_2T_3X_5$ .

## Experimental methods and computational details

### Crystal growth and physical properties

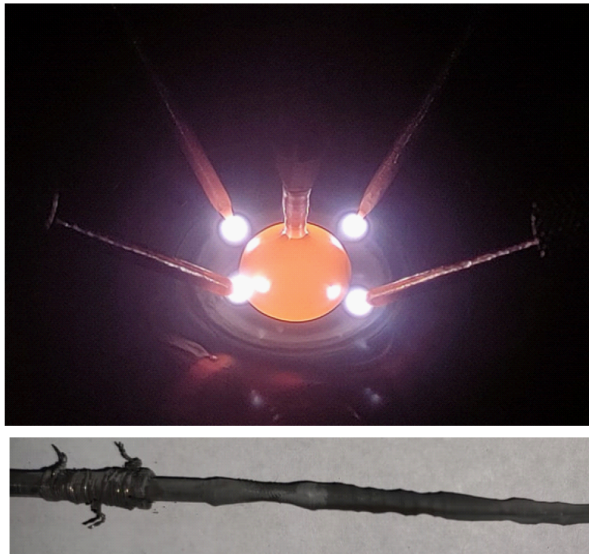


Figure 1: Photograph of the crystal growth process in a tetra-arc furnace and the final pulled ingot.

We have prepared a  $Gd_2Os_3Si_5$  single crystal using the Czochralski method in a tetra-arc furnace (Technosearch Corporation, Japan) under ultra-pure argon atmosphere. The high purity starting elements of Gd, Os, and Si were taken in the molar ratio 2 : 3 : 5 and melted to prepare a polycrystalline ingot of composition  $Gd_2Os_3Si_5$ . The melting process was repeated multiple times to make the sample homogeneous. A seed crystal was

cut from the polycrystalline ingot and used in the Czochralski growth of  $\text{Gd}_2\text{Os}_3\text{Si}_5$ . The seed crystal was gently inserted into the molten solution of  $\text{Gd}_2\text{Os}_3\text{Si}_5$  and pulled rapidly at a rate of 50 mm/h. A necking process was made so that a single crystalline grain is selected for the growth of a single crystal. Once the steady state condition is achieved the crystal was pulled at a rate of 10 mm/h. A snapshot of the crystal growth process is shown in Fig. 1. We obtained a long, rod-shaped ingot with an average diameter of 4 mm and a length of 50 mm as shown in the bottom part of Fig. 1. A Laue diffraction pattern in back-reflection geometry confirmed the single crystalline nature of the pulled ingot as well as its tetragonal symmetry. The structure did not change upon annealing at 1273 K for four days. The composition was confirmed through the energy dispersive X-ray analysis (EDX) attachment in the field emission scanning electron microscope (FESEM) and the anisotropic studies were carried out using commercial equipment like physical property measurement system (PPMS) and superconducting quantum interference device-vibrating sample magnetometer (SQUID-VSM). Detailed explanation for the experimental methods regarding EDX and physical properties are given in the supporting information.<sup>31</sup>

## Temperature-dependent X-ray diffraction

Initially, powder X-ray diffraction (PXRD) was measured at room temperature on an in-house Panalytical X-ray diffractometer, employing  $\text{Cu-K}_\alpha$  radiation. Rietveld refinements of the PXRD data were performed with the FullProf software.<sup>32</sup> Satellite reflections could not be observed in PXRD nor could any lattice distortion away from tetragonal be observed. This result already suggests that the incommensurate CDW modulation is a small deviation from  $P4/mnc$  symmetry.

Single-crystal X-ray diffraction (SXR) experiments were performed on a small piece of crystal of dimensions of  $0.15 \times 0.07 \times 0.1 \text{ mm}^3$ , that was acquired by crushing the large, annealed single crystal. Complete data sets of SXR data were measured at temperatures of 300, 200, 100 and 20 K with a Pilatus 1M CdTe detector. After this cooling run, an

additional data set was measured at 230 K. High-temperature SXR D was measured on a second single crystal, with dimensions:  $0.098 \times 0.026 \times 0.108 \text{ mm}^3$ . The experiment was done on the same diffractometer but with a different detector (Lambda CdTe 7.5 M). Data sets were collected at 400 and 450 K. Both SXR D measurements were carried out employing synchrotron radiation of  $\lambda_{P24} = 0.5 \text{ \AA}$ . Details of both PXR D and SXR D measurements are given in sections S1 and S2 in the supporting information<sup>31</sup>

The EVAL15 software suite<sup>33</sup> was used for processing the SXR D data. SADABS<sup>34</sup> was used for scaling and absorption correction. The latter employed Laue symmetry  $4/mmm$  for the periodic phase and  $mmm$  for the CDW phase. As the crystal structure in the CDW phase is incommensurately modulated we had to use the superspace approach<sup>35-37</sup> to index and integrate the data. The reflection file produced was imported into the software JANA2006 for structure refinement.<sup>38,39</sup> Table 1 gives the crystallographic information at 450 and 400 K (periodic phase), and at 300 and 200 K (incommensurate phase). An unusual criterion of observability was chosen, in order to account for the incorrect estimate of the standard uncertainties in the integrated intensities by the software EVAL15. For details regarding the processing of SXR D data refer to section S3 in the supporting information.<sup>31</sup> Crystallographic tables of other temperatures, and details regarding SXR D data collection and data processing are given in the Supporting Information (SI).<sup>31</sup>

## Electronic structure calculations

Electronic structure calculations were performed within the framework of density functional theory (DFT) as implemented in the Vienna ab initio Simulation Package.<sup>40</sup> We have computed the electronic structure for the tetragonal structure of  $\text{Gd}_2\text{Os}_3\text{Si}_5$  (space group  $P4/mnc$ ). This periodic crystal structure contains 40 atoms (8 Gd atoms, 12 Os atoms and 20 Si atoms) in the primitive unit cell with lattice parameters  $a = 10.706$ ,  $b = 10.706$  and  $c = 5.701 \text{ \AA}$  (compare to the  $C$ -centered setting in Table 1). We used a  $3 \times 3 \times 6$   $\Gamma$ -centered Monkhorst-Pack electronic  $k$ -point mesh, with the plane-wave cut-off energy of 500 eV for



Table 1: Crystallographic data of  $\text{Gd}_2\text{Os}_3\text{Si}_5$  at 450, 400 300 and 200 K. At temperatures 450 and 400 K, the crystal is in the periodic phase and at lower temperatures 300 and 200 K the crystal is in the incommensurate CDW phase.

Temperature (K)	450	400	300	200
Crystal system	Tetragonal	Tetragonal	Orthorhombic	Orthorhombic
Space/Superspace group	$P4/mnc$	$P4/mnc$	$Cccm(\sigma 00)0s0$	$Cccm(\sigma 00)0s0$
Space/Superspace group No. <sup>37</sup>	128	128	66.1.15.8	66.1.15.8
$a$ (Å)	10.7163(2)	10.7122(2)	15.1389(3)	15.1279(3)
$b$ (Å)	10.7163	10.7122	15.1380(2)	15.1271(2)
$c$ (Å)	5.7030(1)	5.7019(3)	5.6998(2)	5.6993(2)
Volume (Å <sup>3</sup> )	654.93(2)	654.30(4)	1306.25(5)	1304.24(5)
Wave vector, $\mathbf{q}_x$	-	-	0.5381(2)	0.5374(3)
$Z$	4	4	8	8
Wavelength (Å)	0.50000	0.50000	0.50000	0.50000
Detector distance (mm)	100	100	110	110
$2\theta$ -offset (deg)	0	0	0	0
$\chi$ -offset (deg)	-60	-60	-60	-60
Rotation per image (deg)	1	1	1	1
$(\sin(\theta)/\lambda)_{max}$ (Å <sup>-1</sup> )	0.712376	0.717144	0.683977	0.683955
Absorption, $\mu$ (mm <sup>-1</sup> )	31.462	31.492	31.549	31.597
$T_{min}$ , $T_{max}$	0.1479, 0.2602	0.1426, 0.2540	0.0216, 0.0534	0.0212, 0.0524
Criterion of observability	$I > 0.75\sigma(I)$	$I > 0.75\sigma(I)$	$I > 0.75\sigma(I)$	$I > 0.75\sigma(I)$
Number of ( $m = 0$ ) reflections measured	9250	9448	5329	5235
unique (obs/all)	542/545	556/558	912/962	908/968
Number of ( $m = 1$ ) reflections measured	-	-	50157	50078
unique (obs/all)	-	-	1529/7648	2104/7630
$R_{int}$ ( $m = 0$ ) (obs/all)	5.27/5.27	5.15/5.15	0.0468/0.0469	0.0460/0.0461
$R_{int}$ ( $m = 1$ ) (obs/all)	-	-	0.0661/0.2700	0.0765/0.2178
No. of parameters	31	31	98	98
$R_F$ ( $m = 0$ ) (obs)	0.0178	0.0185	0.0204	0.0237
$R_F$ ( $m = 1$ ) (obs)	-	-	0.0603	0.0493
$wR_F$ ( $m = 0$ ) (all)	0.0216	0.0223	0.0242	0.0272
$wR_F$ ( $m = 1$ ) (all)	-	-	0.0897	0.0610
$wR_F$ all (all)	0.0216	0.0223	0.0256	0.0284
GoF (obs/all)	1.56/1.56	1.62/1.62	0.83/0.45	0.81/0.49
$\Delta\rho_{min}$ , $\Delta\rho_{max}$ (e Å <sup>-3</sup> )	-3.77, 4.11	-3.71, 3.68	-2.53, 2.15	-2.62, 1.71

the converged results (change in the total electron free energy is  $10^{-3}$  eV/atom when increasing the mesh size to  $4 \times 4 \times 8$  or higher grid density). The convergence criteria for the self-consistent electronic loop was set to  $10^{-8}$  eV. The projector-augmented-wave potentials explicitly included  $5d^14f^7$  states for Gd,  $5d^76s^1$  states for Os and  $3s^23p^2$  for Si as valence electrons.  $\text{Gd}_2\text{Os}_3\text{Si}_5$  undergoes an antiferromagnetic (AFM) transition at  $T_N \sim 5.5$  K, as determined from the electrical resistivity and magnetic susceptibility measurements. Hence, we performed spin-polarized calculations. Spin-orbit coupling (SOC) has minimal influence on ground-state properties; consequently, we did not include SOC in our calculations except for initial testing. We used the generalized gradient approximation (GGA) in the revised Perdew-Burke-Ernzerhof (PBE) parametrization<sup>41</sup> with or without a Hubbard correction.

To account for the localized  $f$  orbitals of Gd atoms and  $d$  orbitals for Os atoms, GGA+ $U$  calculations were used<sup>42</sup> with onsite Coulomb interaction  $U = 6.0$  eV for  $f$  orbitals of Gd atoms and  $U = 2.0$  eV for  $d$  orbitals of Os atoms.<sup>43</sup> On increasing the  $U$  value of Os from 0 to 2 eV, the band structure shifts by nearly 0.1 eV (see Fig. S3 in the SI). The shift has a little influence on the Fermi surface topology and electron susceptibility, as described below. During the relaxation, atomic positions were optimized until forces on all atoms were smaller than 1 meV  $\text{\AA}^{-1}$ . The Fermi surface topology has been calculated by first computing the electron bands on a  $3 \times 3 \times 4$  grid during the self consistent field (SCF) step. Subsequently, we employed the software WANNIER90 (v3.1.0)<sup>44</sup> to compute maximally localized Wannier functions on a 100-orbital basis. The basis included 40  $d$  orbitals of eight Gd atoms and 60  $d$  orbitals of twelve Os atoms in the unit cell, as both significantly contributed to the electronic bands near the Fermi level ( $E_F$ ). To confirm the accuracy of Wannierization, we compared the electronic band structure obtained from the Wannier functions with the direct DFT calculations (see Fig.S4 in SI). We constructed the Fermi surface by evaluating electronic bands on a  $70 \times 70 \times 70$  grid in the entire Brillouin zone using WANNIER90 and plotted it using in-house scripts as shown in Fig. 2.

The electronic susceptibility for a non-interacting Fermi gas, that excludes electron-electron correlations but includes Pauli's exclusion principle can be calculated using the Lindhard function. The first-order perturbative linear response of this gas to a external perturbation of frequency  $\omega$  and wave vector  $\mathbf{q}$  is given by:<sup>45</sup>

$$\chi_0(\mathbf{q}, \omega) = \lim_{\gamma \rightarrow 0} \frac{e^2}{\Omega} \sum_{\mathbf{k}} \sum_{l, l'} \frac{f(\epsilon_{\mathbf{k}+\mathbf{q}, l'}) - f(\epsilon_{\mathbf{k}, l})}{\epsilon_{\mathbf{k}+\mathbf{q}, l'} - \epsilon_{\mathbf{k}, l} - \hbar\omega - i\gamma} |\langle \mathbf{k} + \mathbf{q}, l' | V | \mathbf{k}, l \rangle|^2, \quad (1)$$

where  $e$  is the electron charge,  $\Omega$  is the system volume,  $f(\epsilon_{k,l})$  denotes the electron's Fermi distribution function at energy  $\epsilon$  for a given wave vector  $\mathbf{k}$  and a band index  $l$ ,  $|\langle \mathbf{k} + \mathbf{q}, l' | V | \mathbf{k}, l \rangle|^2$  is the matrix transition element between states  $|\mathbf{k} + \mathbf{q}, l'\rangle$  and  $|\mathbf{k}, l\rangle$ , and  $\gamma$  is a infinitesimal constant. The first and second summations represent the sum over all  $k$

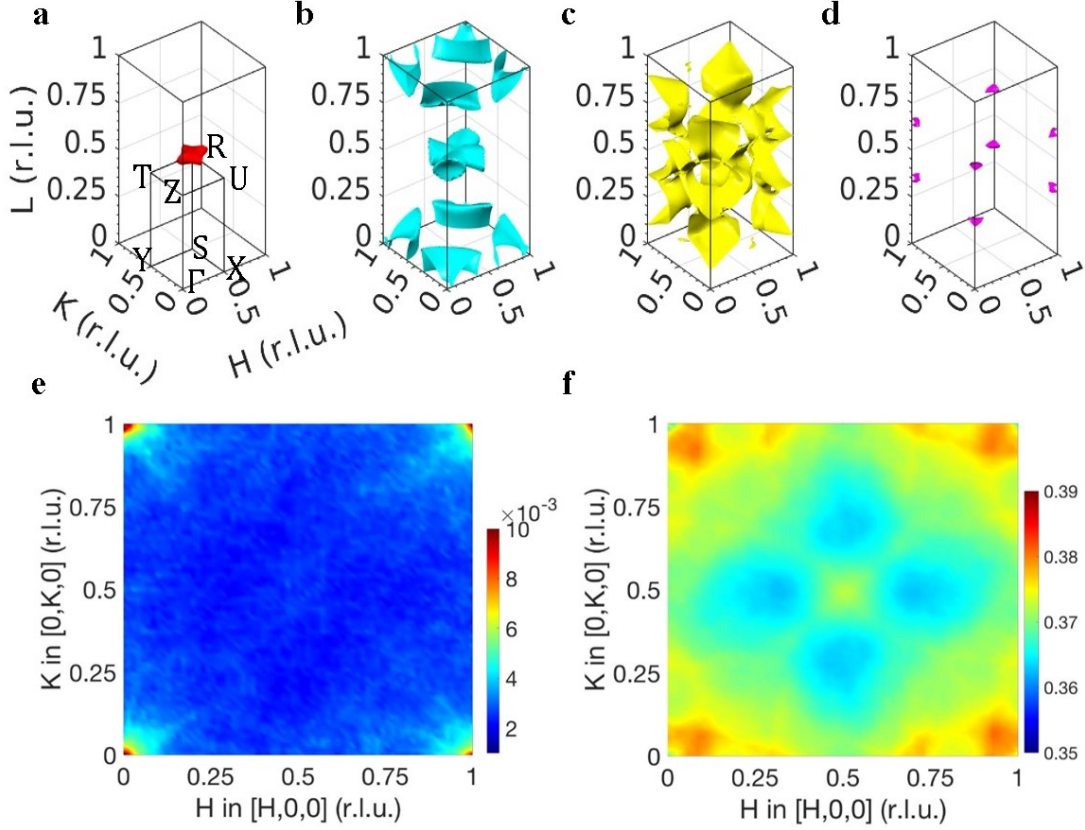


Figure 2: (a-d) Fermi surface topology for  $\text{Gd}_2\text{Os}_3\text{Si}_5$ . Fermi surface is reconstructed from the four bands that cross  $E_F$ . Separate plots of the Fermi surface from different bands are for easy visualization. High-symmetry  $k$ -points of the Brillouin zone are shown in panel (a). r.l.u. refers to the reciprocal lattice units. (e,f) The imaginary and real part of Lindhard susceptibility, i.e.,  $\text{Im}\{\chi_0(\mathbf{q}, \omega)\}$  and  $\text{Re}\{\chi_0(\mathbf{q}, \omega)\}$  for  $\omega = 0$ , in the  $[H, K, 0]$  scattering plane. Colors represent the magnitude of  $\text{Re}\{\chi_0(\mathbf{q}, \omega)\}$  and  $\text{Im}\{\chi_0(\mathbf{q}, \omega)\}$  in arbitrary units. No divergence is visible at experimental CDW wave vectors, thus ruling out any role of Fermi surface nesting and hidden nesting in inducing the CDW.

states and all bands  $l$  in first Brillouin zone, respectively. The real and imaginary part of Lindhard susceptibility are subsequently calculated from Eq. (1) as follows:

$$\text{Re}\{\chi_0(\mathbf{q}, \omega)\} = \lim_{\gamma \rightarrow 0} \frac{e^2}{\Omega} \sum_{\mathbf{k}} \sum_{l, l'} \frac{(\epsilon_{\mathbf{k}+\mathbf{q}, l'} - \epsilon_{\mathbf{k}, l} - \hbar\omega) (f(\epsilon_{\mathbf{k}+\mathbf{q}, l'}) - f(\epsilon_{\mathbf{k}, l}))}{(\epsilon_{\mathbf{k}+\mathbf{q}, l'} - \epsilon_{\mathbf{k}, l} - \hbar\omega)^2 + \gamma^2} \times |\langle \mathbf{k} + \mathbf{q}, l' | V | \mathbf{k}, l \rangle|^2 \quad (2)$$

$$\text{Im}\{\chi_0(\mathbf{q}, \omega)\} = \lim_{\gamma \rightarrow 0} \frac{e^2}{\Omega} \sum_{\mathbf{k}} \sum_{l, l'} \frac{-\gamma (f(\epsilon_{\mathbf{k}+\mathbf{q}, l'}) - f(\epsilon_{\mathbf{k}, l}))}{(\epsilon_{\mathbf{k}+\mathbf{q}, l'} - \epsilon_{\mathbf{k}, l} - \hbar\omega)^2 + \gamma^2} |\langle \mathbf{k} + \mathbf{q}, l' | V | \mathbf{k}, l \rangle|^2. \quad (3)$$

If  $\epsilon_{\mathbf{k}} = \epsilon_{\mathbf{k}+\mathbf{q}} = E_F$ , Eq. (3) reduces to the Fermi surface nesting (FSN) function, where  $E_F$  is the Fermi energy. To evaluate the expressions in Eqs. (2) and (3), certain practical aspects need to be considered. We include bands that lie close to  $E_F$  and contribute to the Lindhard susceptibility, i.e., four bands that cross  $E_F$ . We assume transition matrix elements to be unity, in-line with earlier studies.<sup>46–49</sup> Because of a finite size  $k$ -grid, we use a finite but small value of  $|\gamma| = 1$  meV to broaden the functions with width comparable to the energy difference between the discrete  $k$  points (although because of this we sacrifice some fine structure).  $\text{Re}\{\chi_0(\mathbf{q}, \omega)\}$  and  $\text{Im}\{\chi_0(\mathbf{q}, \omega)\}$  for  $\omega = 0$  in the  $(H, K, 0)$  scattering plane is shown in Fig. 2(e,f).

## Results and Discussion

### Incommensurately modulated structure of the CDW state

According to the present SXRD experiments,  $\text{Gd}_2\text{Os}_3\text{Si}_5$  adopts the tetragonal  $\text{Sc}_2\text{Fe}_3\text{Si}_5$  structure type for temperatures 450 and 400 K (Figs. 3 and 4). The observed scattering near the satellite positions in the SXRD at 400 K is diffuse scattering (Fig. 3) and it indicates CDW fluctuation above  $T_{\text{CDW}}$ . Diffuse scattering at temperatures above  $T_{\text{CDW}}$  has been observed for other CDW systems too.<sup>50</sup> The symmetry of the periodic phase is given by the space group  $P4/mnc$ , much like  $RE_2\text{Re}_3\text{Si}_5$  ( $RE = \text{Ce}, \text{Pr}, \text{Ho}$ )<sup>24,25</sup> and  $RE_2\text{Ru}_3\text{Ge}_5$  ( $RE = \text{Dy}, \text{Sm}, \text{Pr}$ ).<sup>7</sup> Structure refinements led to an excellent fit to the SXRD data (Table 1). Structural parameters are provided in Table S5 in the Supplementary Material.<sup>31</sup>

For temperatures 300 K and below, SXRD has indicated the presence of Bragg reflections in addition to those of the  $\text{Sc}_2\text{Fe}_3\text{Si}_5$  structure type. These reflections can be indexed as incommensurate satellite reflections (Fig. 5). They are evidence for an incommensurately modulated structure. This structure has been determined by structure refinements within the superspace approach (Table 1).

We did not observe any distortion of the tetragonal lattice of the average structure.

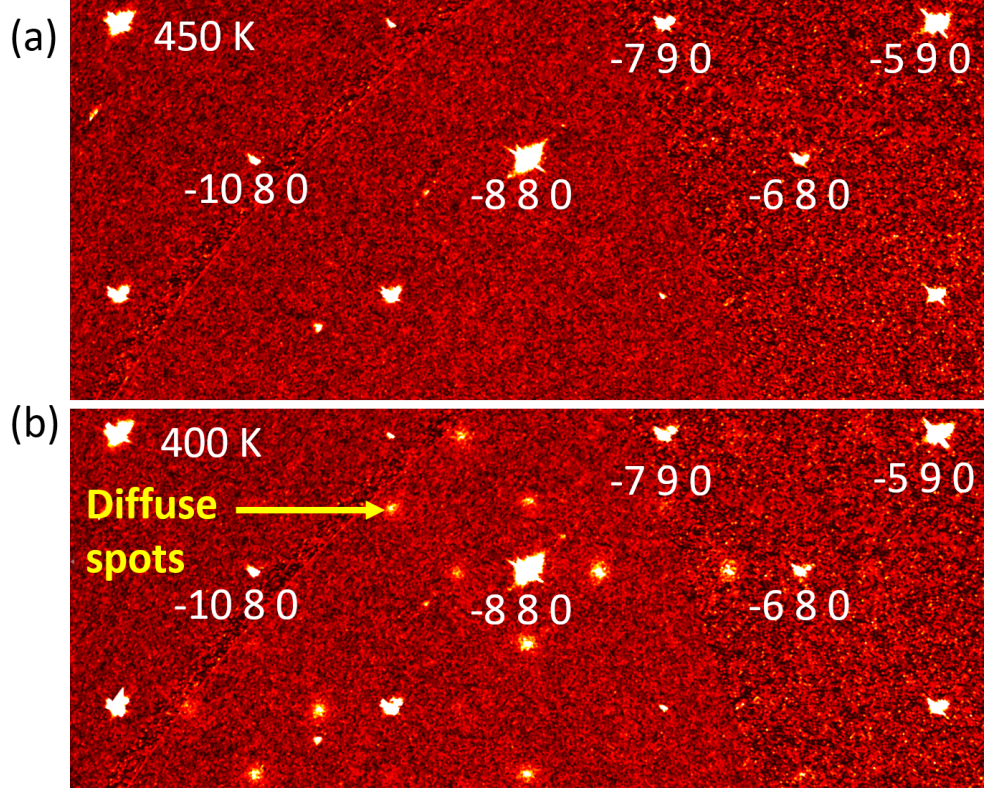


Figure 3: Excerpts of the reconstructed reciprocal layers ( $hk0$ ) of diffraction, for temperatures of (a) 450 K and (b) 400 K. Indices are given for several main reflections according to the  $C$ -centered setting. These diffuse spots indicated by a yellow arrow, become satellite reflections at lower temperatures, as shown in Fig. 5.

Furthermore, the observed modulation wave vectors obey the tetragonal symmetry according to

$$\begin{aligned}
 \mathbf{q}^1 &= (\sigma_1, \sigma_1, 0) \\
 \mathbf{q}^2 &= (-\sigma_1, \sigma_1, 0)
 \end{aligned} \tag{4}$$

with  $\sigma_1 = 0.2691(3)$  at  $T = 300$  K. Here, the fourfold rotation transforms  $\mathbf{q}^1$  into  $\pm\mathbf{q}^2$ , and  $\mathbf{q}^2$  into  $\mp\mathbf{q}^1$ . An immediate choice for the symmetry of the incommensurately modulated structure would thus be a (3+2)-dimensional  $[(3+2)D]$  superspace group based on the tetragonal space group  $P4/mnc$  of the average structure together with the two modulation wave vectors of Eq. 4. However, these models failed to describe the intensities of the satellite

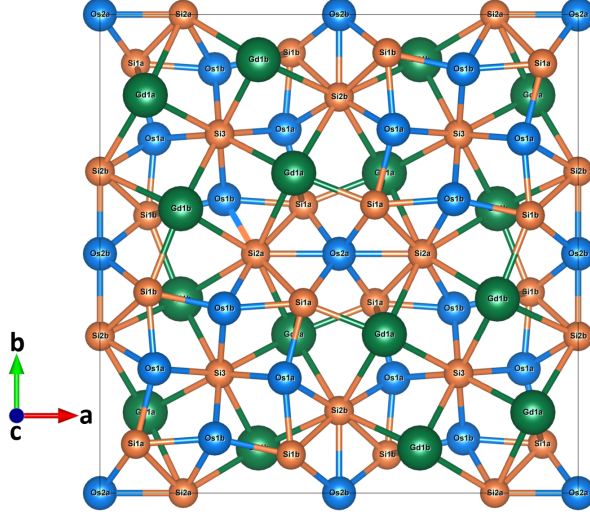


Figure 4: Projection onto the  $(ab)$ -plane of the average crystal structure of  $\text{Gd}_2\text{Os}_3\text{Si}_5$  at 300 K, depicting one  $C$ -centered unit cell. Large green spheres correspond to gadolinium, blue spheres of intermediate sizes correspond to osmium and small orange spheres depict silicon. Atom numbers are indicated.

reflections. See model A in Table 2.

Table 2: Crystallographic data of three structure models for the incommensurate CDW phase at  $T = 200$  K. Criterion of observability of Bragg reflections is:  $I > 0.75\sigma(I)$ .

Model	A	B	C	D
Crystal system	Tetragonal	Tetragonal	Orthorhombic	Orthorhombic
Superspace group	$P4/mnc(\sigma\sigma 0)0000$ $(-\sigma\sigma 0)0000$	$P4/m(\sigma_1\sigma_2 0)0000$ $(-\sigma_2\sigma_1 0)0000$	$Pnmm(\sigma_1\sigma_2 0)000$ $(-\sigma_1\sigma_2 0)000$	$Cccm(\sigma 00)0s0$
Superspace group No. <sup>37</sup>	128.2.68.5	83.2.57.1	58.2.50.13	66.1.15.8
$a$ (Å)	10.7042(2)	10.7042(2)	10.7042(2)	15.1279(3)
$b$ (Å)	10.7042	10.7042	10.7042(2)	15.1271(2)
$c$ (Å)	5.6993(2)	5.6993(2)	5.6995(3)	5.6993(2)
Volume (Å <sup>3</sup> )	653.03(5)	653.03(5)	653.05(5)	1304.24(5)
Wave vector, $\mathbf{q}^1$	(0.2691(3), 0.2691(3), 0)	(0.2691(3), 0.2691(3), 0)	(0.2691(3), 0.2691(3), 0)	(0.5374(3), 0, 0)
Wave vector, $\mathbf{q}^2$	(-0.2691(3), 0.2691(3), 0)	(-0.2691(3), 0.2691(3), 0)	(-0.2691(3), 0.2691(3), 0)	-
$Z$	4	4	4	8
Laue symmetry	$4/mmm$	$4/m$	$mmm$	$mmm$
$R_{int}$ (all)(obs)	0.0500	0.0461	0.0446	0.0467
$R_{int}(m=0)$ (obs)	0.0486	0.0453	0.0437	0.0460
$R_{int}(m=1)$ (obs)	0.0879	0.0737	0.0758	0.0765
No. of parameters	66	131	130	98
$R_F(m=0)$ (obs)	0.0233	0.0248	0.0227	0.0237
$R_F(m=1)$ (obs)	0.5315	0.0591	0.0583	0.0493
$wR_F(m=0)$ (all)	0.0256	0.0276	0.0263	0.0272
$wR_F(m=1)$ (all)	0.6061	0.0680	0.0655	0.0610
$wR_F$ all (all)	0.1036	0.0291	0.0279	0.0284
GoF (obs/all)	3.18/2.12	0.84/0.49	0.84/0.49	0.81/0.49
$\Delta\rho_{min}, \Delta\rho_{max}$ (e Å <sup>-3</sup> )	-19.43, 19.41	-2.77, 2.41	-3.05, 1.74	-2.62, 1.71

Model B refers to a lowering of the average symmetry towards tetragonal  $P4/m$ , which is a subgroup of index two of  $P4/mnc$ . This symmetry lowering introduces the possibility of

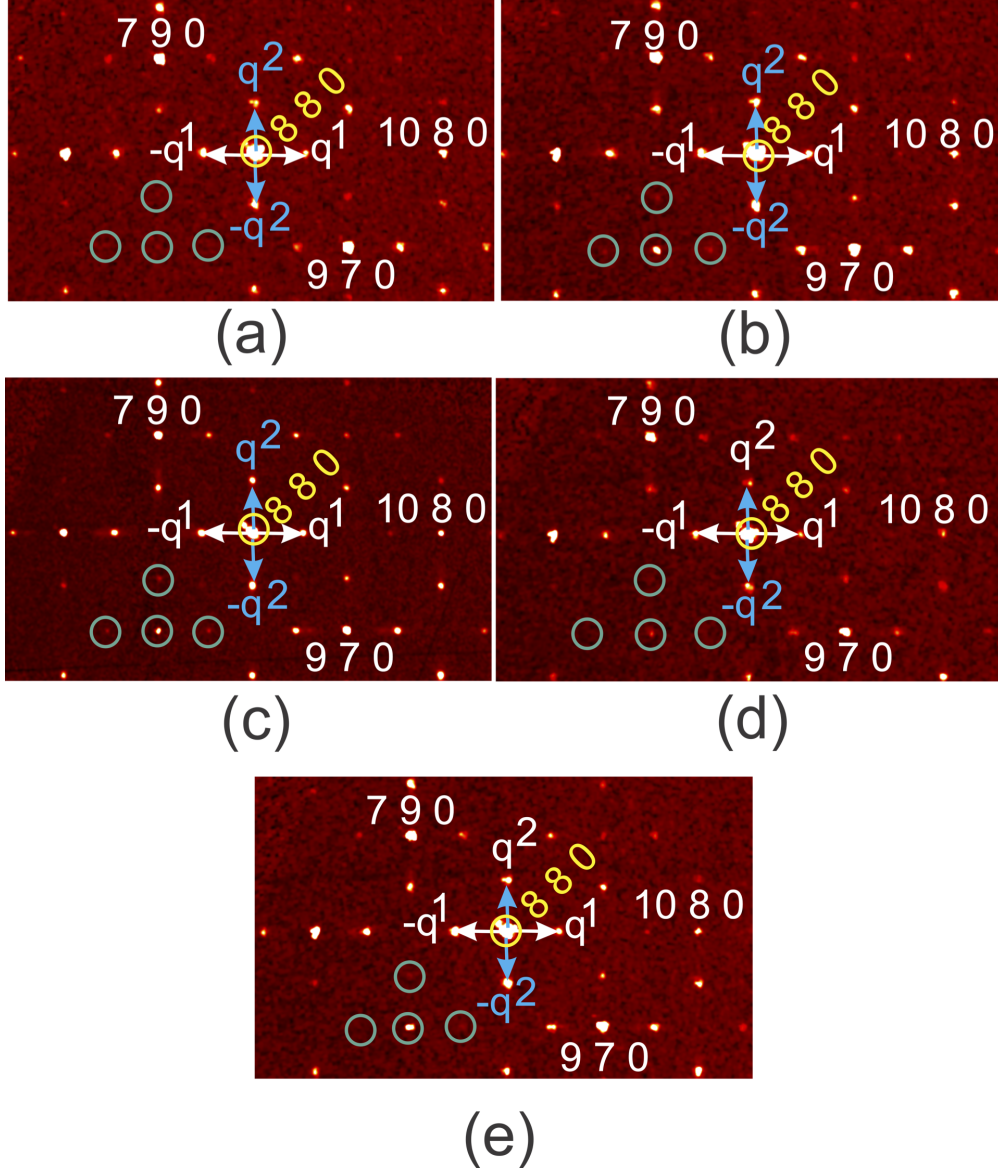


Figure 5: Reconstructed reciprocal layers ( $hk0$ ) of SXRD measured at temperatures of (a) 300 K, (b) 230 K, (c) 200 K, (d) 100 K, and (e) 20 K. Indices are given for several main reflections and satellite reflections according to the  $C$ -centered setting. The yellow circles highlight the main reflection (880). It is surrounded by four superlattice reflections, whose positions are defined by  $\pm\mathbf{q}^1$  and  $\pm\mathbf{q}^2$  (Eq. 4).  $\mathbf{q}^1$  and  $\mathbf{q}^2$  are related by twinning. Green circles indicate weakening of reflections at around 100 K (see Fig. 6(d) for details.)

twinning with two domains.<sup>27</sup> The modulation remains 2D, but the modulation wave vectors now have two independent unrestricted components, although experimental values indicate them to be equal. Crystal structure refinements led to a good fit to the diffraction data. See model B in Table 2.

Another subgroup of  $P4/mnc$  is the orthorhombic space group  $Pnmm$ . The modulation remains 2D. Model C with the (3+2)D superspace group symmetry based on  $Pnmm$  provides a fit of similar quality as model B (Table 2).

As final option we have considered structures with 1D modulations, where each domain is modulated with either  $\mathbf{q}^1$  or  $\mathbf{q}^2$ . This choice of symmetry is motivated by the failure to observe mixed-order satellite reflections at  $\mathbf{q}^1 \pm \mathbf{q}^2$ . The highest such possible symmetry is the orthorhombic subgroup  $Cccm$  of  $P4/mnc$ . Structure refinements with a (3+1)D superspace group based on the average-structure symmetry  $Cccm$  led to the best fit to the diffraction data. See model D in Table 2. An additional argument in favor of model D is that the lower  $R$  values are obtained for a model with a considerably smaller number of parameters for model D than for models B or C (Table 2).

Table S4 in the Supplementary Material<sup>31</sup> gives an overview of  $R$  values for a total of 26 possible superspace symmetries. It reveals that the best fit to the SXRD data is indeed found for model D with  $Cccm(\sigma 00)0s0$ . Non-centrosymmetric subgroups lead to nearly equal  $R$  values, while the number of parameters is 1.6–2 times larger. The present SXRD data thus indicate a centrosymmetric CDW in  $Gd_2Os_3Si_5$ .

Based on these considerations, we propose for the incommensurately modulated phase of  $Gd_2Os_3Si_5$  a structure model involving a 1D modulation and Superspace symmetry  $Cccm(\sigma 00)0s0$ . Structural parameters are provided in Tables S6 and S7 in the Supplementary Material.<sup>31</sup>

At all measured temperatures within the range 20–300 K, the lattice parameters of the average structure obey tetragonal symmetry restrictions (Fig. 6), although the modulated structure clearly is orthorhombic. Only a few cases are known, for which the lowering of the crystal symmetry is entirely due to the modulation of atomic positions, including the CDW compounds  $CuV_2S_4$ ,  $EuAl_4$ ,  $Sm_2Ru_3Ge_5$  and  $SrAl_4$ .<sup>7,51–53</sup>

We have not observed a lock-in transition down to 20 K [Fig. 6(c)]. In most cases, the intensities of superlattice reflections should increase with decreasing temperature, because of an increasing strength of the modulation. However, we presently find a reduction of the



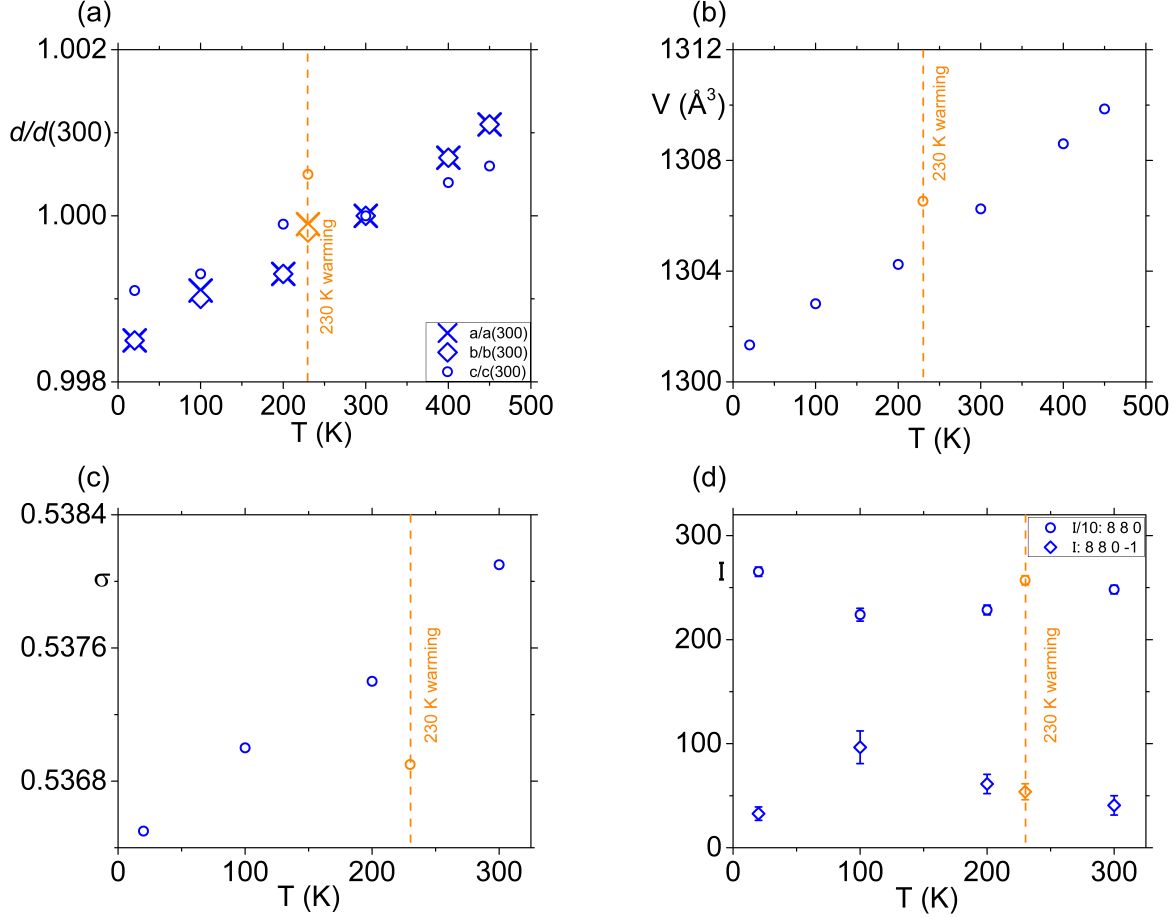


Figure 6: (a) values of the lattice parameters relative to their values at 300 K; with  $a(300) = 15.1389(3)$ ,  $b(300) = 15.1380(2)$ , and  $c(300) = 5.6998(2)$  ( $\text{\AA}$ ). (b) Unit cell volume. (c) Component  $\sigma$  of  $\mathbf{q}$ . (d) Intensity of main reflection (880) and satellite reflection (880-1) as a function of temperature. The data were recorded during cooling, except those measured at 230 K (marked by a dashed line) that were recorded during heating of the sample. 450 and 400 K are in the tetragonal phase, while lower temperatures from 300 K to 20 K are in the orthorhombic CDW phase.

intensity of satellite reflections below 100 K [Fig. 6(d)]. This observation represents a similar trend as reported for  $\text{Sm}_2\text{Ru}_3\text{Ge}_5$ .<sup>7</sup>

Isostructural  $\text{Gd}_2\text{Os}_3\text{Si}_5$  and  $\text{Sm}_2\text{Ru}_3\text{Ge}_5$  compounds feature similar modulation wave vectors. Bugaris *et al.*<sup>7</sup> have reported a modulated crystal structure for  $\text{Sm}_2\text{Ru}_3\text{Ge}_5$ , which has monoclinic symmetry with the (3+1)D superspace group  $Pm(\alpha 0 \gamma)0$  (Table 3). Here, the average-structure space group  $Pm$  is a subgroup of  $P4/mnc$ , where the mirror perpendicular to the tetragonal axis is preserved in the monoclinic symmetry. Motivated by

Table 3: Crystallographic information on the monoclinic and orthorhombic structure models for the incommensurate CDW phase of  $\text{Sm}_2\text{Ru}_3\text{Ge}_5$  at 100 K.

Chemical formula	$\text{Sm}_2\text{Ru}_3\text{Ge}_5$	
	${}^a Pm(\alpha 0 \gamma)0$	${}^b Cccm(\sigma 0 0)0s0$
Superspace group		
No. <sup>37</sup>	6.1.2.1	66.1.15.18
$a$ (Å)	10.9955(2)	15.5491(2)
$b$ (Å)	5.7823(3)	15.5493(3)
$c$ (Å)	10.9942(3)	5.7823(3)
$\alpha$ (deg)	90	90
$\beta$ (deg)	90	90
$\gamma$ (deg)	90	90
Volume (Å <sup>3</sup> )	699.00(4)	1398.31(4)
Modulation wave vector		
$\sigma_1$	0.219(5)	0.4380(5)
$\sigma_2$	0	0
$\sigma_3$	0.219(4)	0
$Z$	4	8
Criterion of observability	$I > 2\sigma(I)$	$I > 2\sigma(I)$
Independent	17468	17112
No. of parameters	617	97
$R_F$ ( $m = 0$ ) (obs/all)	0.0607/0.0609	0.0574/0.0576
$R_F$ ( $m = 1$ ) (obs/all)	0.1207/0.2730	0.1528/0.3058
$wR_F$ ( $m = 0$ ) (all)	0.1704	0.1097
$wR_F$ ( $m = 1$ ) (all)	0.3011	0.2211
$wR_F$ all (all)	0.1752	0.1211

<sup>a</sup>Information taken from Bugaris *et al.*<sup>7</sup>

<sup>b</sup>Structure refinements against SXR data kindly supplied by Bugaris *et al.*<sup>7</sup>

their similar average crystal structures, we have refined a structure model with orthorhombic  $Cccm(\sigma 0 0)0s0$  symmetry against the diffraction data from Bugaris *et al.*<sup>7</sup> for  $\text{Sm}_2\text{Ru}_3\text{Ge}_5$  (Table 3). Whereas the fit to the main reflections is the same for the monoclinic and orthorhombic structure models, the fit to the satellite reflections is worse for orthorhombic symmetry. However, the monoclinic model has 617 parameters, whereas the orthorhombic model only needs 97 parameters. Secondly, neither  $R_F^{obs}(m = 1) = 0.121$  nor  $R_F^{obs}(m = 1) = 0.15$  represent good fits to the satellite reflection intensities. Considering the massive increase in number of parameters upon lowering the symmetry from  $Cccm$  towards  $Pm$ , we believe that there is no conclusive evidence for either structure model. A structure with superspace symmetry  $Cccm(\sigma 0 0)0s0$  thus is quite well possible for the CDW phase of  $\text{Sm}_2\text{Ru}_3\text{Ge}_5$ .

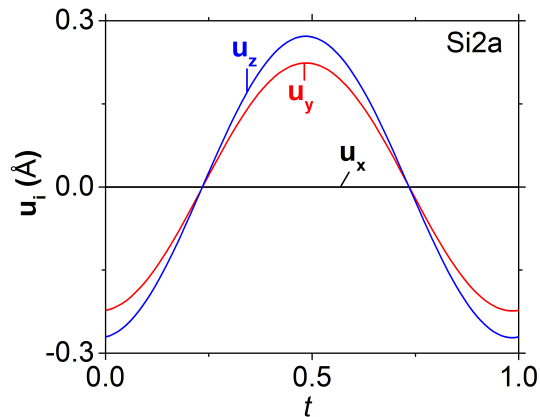


Figure 7:  $t$ -plot of displacement modulation of Si2a at 200 K.

### Location of the CDW in $\text{Gd}_2\text{Os}_3\text{Si}_5$

The tetragonal crystal structure with symmetry  $P4/mnc$  involves six crystallographically independent atoms, Gd1, Os1, Os2, Si1, Si2 and Si3 respectively. The basic structure of the incommensurately modulated CDW structure possesses the symmetry  $Cccm$ . Employing group-subgroup relations, one finds that five out of these six sites split into two independent positions, enumerated by Gd1a, Gd1b, Os1a, Os1b, Os2a, Os2b, Si1a, Si1b, Si2a, Si2b and Si3. Their positions in the  $C$ -centered unit cell are shown in Fig. 4. Deviations from tetragonal symmetry are very small for the refined basic-structure coordinates (Table S6 in<sup>31</sup>).

Inspection of the list of modulation amplitudes reveals that by far the largest displacements are those of the Si2a atom (Table S7 in<sup>31</sup>). Specifically, large displacements of Si2a are found along  $\mathbf{b}$  and  $\mathbf{c}$  (Fig. 7), while Si2b has small displacements. This feature demonstrates the deviation from tetragonal symmetry of the CDW modulation, since tetragonal symmetry would imply equal magnitudes of the amplitudes for Si2a and Si2b atoms. Accordingly, the modulation mainly affects bonding around Si2a atoms (Fig. 8).

Specifically, major variations are found for the distances Gd1a-Si2a and Gd1b-Si2a, and to a lesser extent for the distance Os1b-Si2a, while the Os2a-Si2a bond is almost not modulated. A large variation is found for the Si2a-Si2a bonding contact (Fig. 9).

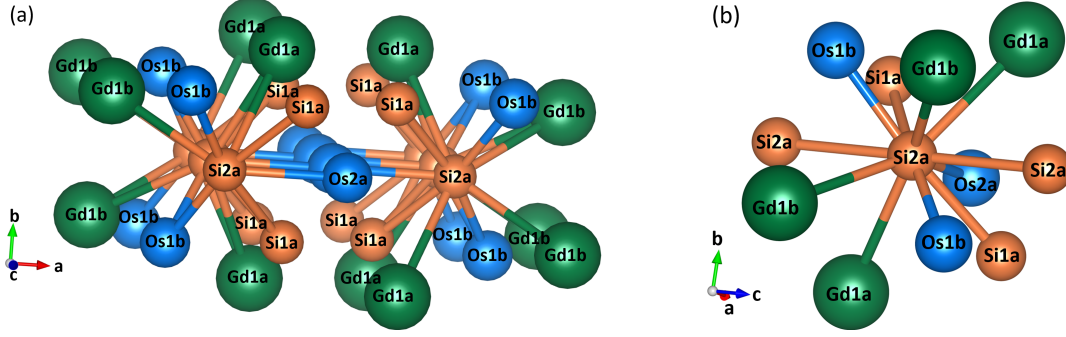


Figure 8: (a) Extended view of the coordination of the Si2a atom. (b) The eleven atoms in the first coordination sphere of Si2a. Neighboring atoms are  $2 \times \text{Gd1a}$ ,  $2 \times \text{Gd1b}$ ,  $2 \times \text{Os1b}$ ,  $1 \times \text{Os2a}$ ,  $2 \times \text{Si1a}$ ,  $2 \times \text{Si2a}$ .  $t$ -Plots of the variations of these distances in the modulated structure are provided in Fig. 9.

Specifically, large variations are found for the four Si2a–Gd contacts, while the largest variation is obtained for the distances to the two Si2a neighbours of Si2a (Fig. 9). The variation of contact distances is in phase for three contacts Si2a, Gd1a and Gd1b, while they are out of phase with the other group of three Si2a, Gd1a and Gd1b atoms (Fig. 9). A complete set of  $t$ -plots of short interatomic distances is given in the Supporting Information.<sup>31</sup> The gadolinium and osmium atoms are too far apart from each other for a significant direct interaction between them. This indicates that the CDW deviates from typical CDW systems, as they do not involve metal-metal contacts, since the CDW in  $\text{Gd}_2\text{Os}_3\text{Si}_5$  is caused by Si2a atoms. This is in contrast to the  $\text{RE}_2\text{Ir}_3\text{Si}_5$  systems ( $\text{R} = \text{Lu}, \text{Er}, \text{Ho}$ ) which are orthorhombic as the CDW involves the Ir atoms and the Si atoms. For detailed comparison of the CDW in the tetragonal and orthorhombic variants refer to section S8 in the Supporting information.<sup>31</sup>

## Origin of the CDW in $\text{Gd}_2\text{Os}_3\text{Si}_5$

As described above, the CDW in  $\text{Gd}_2\text{Os}_3\text{Si}_5$  involves the modulation of Si atoms as opposed to Ir–Ir zig-zag chains in  $\text{Ho}_2\text{Ir}_3\text{Si}_5$ <sup>17</sup> or Ge–Ge zig-zag chains in  $\text{Sm}_2\text{Ru}_3\text{Ge}_5$ .<sup>7</sup> A CDW can be stabilized by one of several mechanisms.<sup>50</sup> These include Fermi surface nesting and hidden nesting,<sup>45–49,54–56</sup> wave vector-dependent electron-phonon coupling,<sup>57–60</sup> strong electron

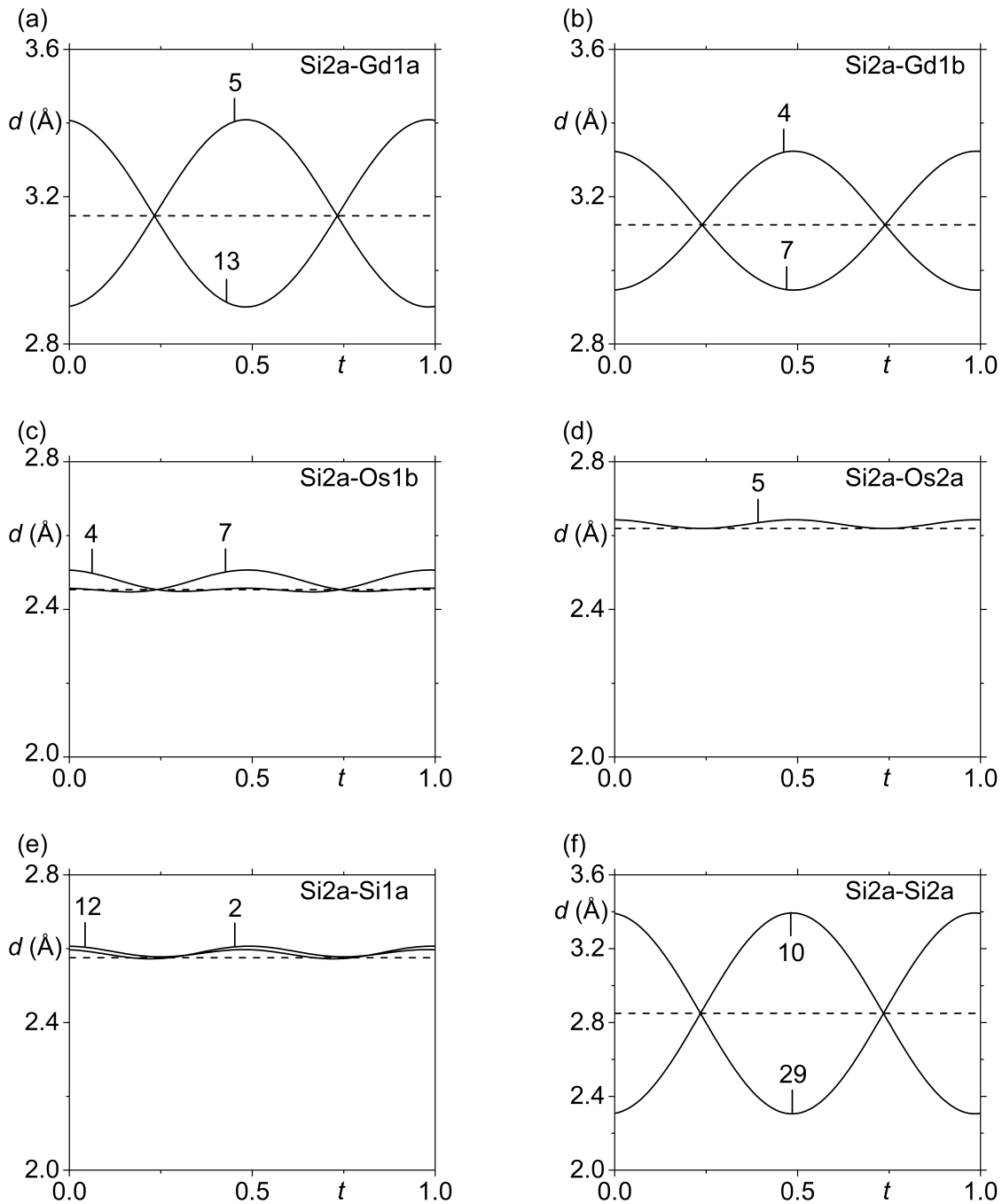


Figure 9:  $t$ -Plots of interatomic distances  $d$  (Å) of Si2a–Gd1a, Si2a–Gd1b, Si2a–Os1b, Si2a–Os2a, Si2a–Si1a and Si2a–Si2a at 200 K. All plots refer to a single Si2a atom; compare to Fig. 8.  $t$ -Plots display interatomic distances as a function of the phase  $t$  of the modulation wave.<sup>35</sup> The number on each curve is the number of the symmetry operator that is applied to the coordinating atom. Symmetry operators are listed in Table S9 in the Supplemental Material.<sup>31</sup>

correlations,<sup>47,61,62</sup> and a large electronic density of states (EDOS) near the Fermi level ( $E_F$ ) having degenerate branches.<sup>63,64</sup>

We have calculated the electronic band structure of  $\text{Gd}_2\text{Os}_3\text{Si}_5$ , and thus obtained the Fermi surface, and the Lindhard susceptibility in the static limit ( $\omega = 0$ ), with real part  $\text{Re}\{\chi_0(\mathbf{q}, \omega)\}$  and imaginary part  $\text{Im}\{\chi_0(\mathbf{q}, \omega)\}$ . Figure S5 shows the orbital- and atom-resolved electronic band structure and EDOS. As one can observe, the states near  $E_F$  are primarily formed by Gd- $d$  and Os- $d$  orbitals with little contribution from Si- $p$  orbitals. Importantly, the EDOS at  $E_F$  is relatively low, thus ruling out a large EDOS at  $E_F$  to be the governing mechanism for CDW formation, the latter which is quite prevalent in the actinides.<sup>63,64</sup>

Furthermore, we control the electron correlations by increasing the Coulomb interaction parameter  $U$  from 0 to 2 eV for Os atoms in calculations which have significant contribution near  $E_F$ , but the band structure rigidly shifts by  $\sim 0.1$  eV with little influence on Fermi surface topology and electron susceptibility (Fig.S3). Hence strong electron correlations are unlikely to play governing role in the formation of the CDW in  $\text{Gd}_2\text{Os}_3\text{Si}_5$ .

Next, we evaluate Fermi surface nesting and hidden nesting. Figure 2(a-d) shows the Fermi surface where multiple electron and hole pockets can be seen. On visual inspection, some parallel contours separated by a finite wave vector are visible in Fig. 2(b) and 2(c). We have calculated  $\text{Im}\{\chi_0(\mathbf{q}, \omega)\}$  to identify whether the parallel contours will lead to divergence, a signature of Fermi surface nesting mechanism.<sup>45-49,54-56</sup> Figure 2(e) displays  $\text{Im}\{\chi_0(\mathbf{q}, \omega)\}$  in the  $(H, K, 0)$  scattering plane that shows the divergence near zero wave vectors only (i.e., at the corners); hence pointing towards the absence of finite wave vector CDW driven by Fermi surface nesting. Moreover, since electronic bands disperse linearly near  $E_F$  (Fig. S4(b)), it is possible, similar to  $\alpha$ -U and  $\text{EuTe}_4$ ,<sup>48,49</sup> that hidden nesting may drive the CDW transition here. To explicitly confirm the role of hidden nesting, we further calculate  $\text{Re}\{\chi_0(\mathbf{q}, \omega)\}$  as shown in Fig. 2(f). We obtain weak divergence near zero wave vectors but no divergence at experimentally obtained CDW wave vector in  $\text{Gd}_2\text{Os}_3\text{Si}_5$ . Note

that, as discussed earlier, since the CDW involves modulation of Si atoms which have little contribution near  $E_F$ , it is reassuring that our calculations explicitly confirm that nesting nor strong correlations of Gd and Os bands would control the formation of CDW. From the above analysis, it seems likely that wave vector-dependent electron-phonon coupling is the dominant mechanism in  $\text{Gd}_2\text{Os}_3\text{Si}_5$ , where electronic states near  $E_F$  interact with a phonon branch involving Si displacements at CDW wave vector to induce phonon softening; and subsequently, the freezing of Si vibrations below  $T_{\text{CDW}}$  at CDW wave vector leads to the formation of CDW observed in experiments. Due to the large unit cell (40 atoms) and 100-orbital basis required to reproduce bands near  $E_F$ , it remains challenging to confirm the wave vector-dependent electron-phonon coupling mechanism theoretically.

## Physical Properties and the CDW phase transition

Figure 10 shows the temperature dependence of electrical resistivity  $\rho(T)$  for current ( $J$ ) along the two principal crystallographic directions,  $\mathbf{a}$  and  $\mathbf{c}$ , for the cooling and warming cycles in the temperature range 370 to 2 K. For  $J_{\mathbf{a}}$ ,  $\rho(T)$  increases with decrease in the

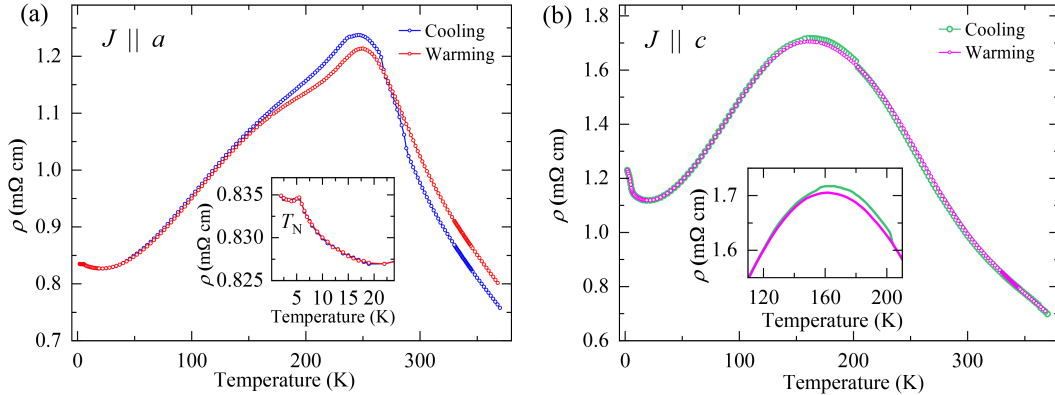


Figure 10: Temperature dependent electrical resistivity during cooling and warming cycles for (a)  $J_{\mathbf{a}} \parallel \mathbf{a}$ , and (b)  $J_{\mathbf{c}} \parallel \mathbf{c}$ , insets show the expanded view at low temperatures.

temperature down to 250 K for both cooling and warming cycles, showing semiconducting behavior.  $\rho(T)$  decreases with further decrease of the temperature with change in the slope near 220 K and a broad hump around 150 K. There is a subtle increase in  $\rho(T)$  below 20 K due

to enhanced spin-disorder scattering, which is confirmed from  $\chi(T)$  as discussed later.  $\rho(T)$  suddenly drops in the magnetically ordered state below  $T_N \sim 5.5$  K. This shows a metallic behavior in the temperature range 250 to 2 K, and semiconducting behavior between 370 and 250 K. Note that the cooling data exhibits higher resistivity than the warming cycle between 100 and 270 K. Above 270 K, the warming data obtains higher resistivity values. As a result, there are two hysteresis loops, for 100 to 270 K and for 270 to 370 K and above, in the cooling and warming runs [Fig. 10(a)]. Below 100 K, both cooling and warming curves more or less collapse onto a single curve along with a broad hump around 150 K.

For  $J_c$ ,  $\rho(T)$  increases with decreasing temperature down to  $\sim 170$  K, showing semiconducting behavior. Further decrease in the temperature between 150 to 20 K,  $\rho(T)$  decreases. It shows a broad hump at around 160 K. Unlike the case of  $J_a$ ,  $\rho(T)$  below  $T_N \sim 5.5$  K increases with decrease in the temperature, which may be attributed to the magnetic superzone gap. We can see a significant hysteresis between cooling and warming runs between 140 to 205 K (inset of Fig 10(b)). These warming and cooling curves do not collapse onto a single curve for temperatures up to 370 K, while a hysteresis is observed. From the  $\rho(T)$  analysis, we can state that there are two main features: (i) insulator to metal transition (IMT), and (ii) hysteresis in cooling and warming cycles in the metallic as well as the insulating regimes. The IMT along with hysteresis appears to indicate CDW phase that is in line with observed superlattice peaks in SXRD. Hysteresis in cooling and warming cycles in the metallic regime may associate with the structural phase transition. However, we did not find any change in the modulated structure below 300 K from the SXRD data. At the same time, superlattice reflections are pronounced in the hysteretic regime, which suggests that there may be successive CDW states in this compound.

The temperature-dependent magnetic susceptibility  $\chi(T)$  has been measured during field-cooled cooling (FCC) and zero-field-cooled (ZFC) protocols, in an applied magnetic field of  $H = 50$  Oe for the field parallel to  $\mathbf{a}$  ( $\chi_a(T)$ ) and parallel to  $\mathbf{c}$  ( $\chi_c(T)$ ) [Fig. 11(a,b)]. In FCC, the data were recorded during cooling cycle of the sample from 390 to 1.8 K. In ZFC,



the data were recorded during warming cycle from 1.8 to 390 K, after cooling the sample in zero field. The magnetic susceptibility exhibits anomalies in both  $\chi_a(T)$  and  $\chi_c(T)$  at  $T_N \simeq 5.5$  K, due to long-range antiferromagnetic order below  $T_N$ . Above  $T_N$ ,  $\chi_a(T)$  and  $\chi_c(T)$  decreases with increasing temperature, with no sign of anisotropy as expected for a  $S$ -state Gd-ion.

We have obtained a good fit of the Curie-Weiss (CW) law to both the data  $\chi_a(T)$  and the data  $\chi_c(T)$  of the ZFC protocol, in the temperature range 100 – 320 K (Fig. 11(a,b), insets). These fits resulted in  $\mu_{\text{eff}} = 7.9 \mu_B/\text{Gd}$  for both the directions, a value which is close

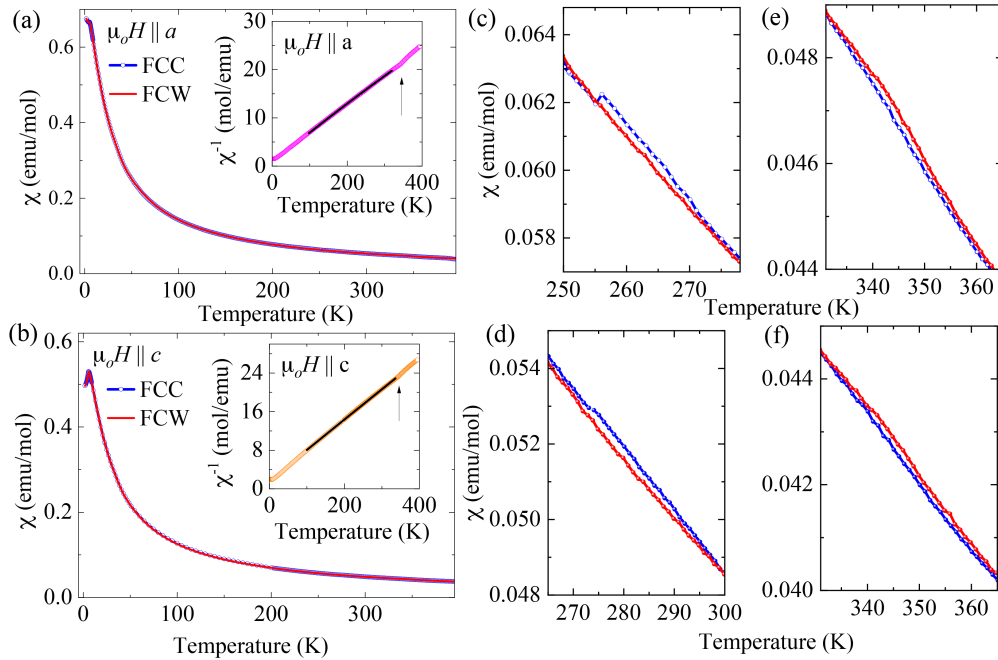


Figure 11: (a) Temperature dependent magnetic susceptibility during FCC and ZFC runs of  $\text{Gd}_2\text{Os}_3\text{Si}_5$  for (a)  $\mu_0 H \parallel \mathbf{a}$  and (b)  $\mu_0 H \parallel \mathbf{c}$  at 50 Oe. Expanded view of susceptibility at different temperature regimes for (c, e)  $\mu_0 H \parallel \mathbf{a}$  and (d, f)  $\mu_0 H \parallel \mathbf{c}$ . Insets (a, b) show Curie-Weiss (CW) fitting in the temperature range 100-320 K.

to the theoretical value of  $7.94 \mu_B/\text{Gd}$  for  $\text{Gd}^{3+}$ . Interestingly, there is a change in slope of the  $\chi^{-1}(T)$  vs  $T$  plots at  $T = 345$  K, which we interpret as the signature of a CDW phase transition.

The magnetic susceptibility exhibits hysteresis for FCC and ZFC runs between 255 and 270 K for  $\chi_a(T)$ , and between 265 and 300 K for  $\chi_c(T)$  [Fig. 11(c,d)]. Such a hysteretic

behavior is also seen in  $\rho(T)$  in cooling and warming cycles for  $J_a$  (Fig. 10(a)). A second measurement on the same sample led to a hysteresis in  $\chi_a(T)$  of 260–285 K [the inset in Fig. S2(a)], and of 335–370 K (the inset in Fig. S2(b)). The slightly different temperature ranges are attributed to different thermal histories of the sample, when the two measurements were performed.

Notably, the inverse magnetic susceptibility exhibits a change in the slope near 345 K for both  $\chi_a(T)$  and  $\chi_c(T)$  [inset in Fig. 11(a,b)]. An expanded view of  $\chi_a(T)$  and  $\chi_c(T)$  reveals a small hysteresis for 330 to 365 K [Fig. 11(e,f)]. We believe that this high temperature anomaly at  $T_{\text{CDW}} \sim 345$  K is associated with the CDW phase transition. This value for  $T_{\text{CDW}}$  is in agreement with the results from high-temperature SXRD (Section ).

## **Criterion for the formation of CDW/structural transitions in $RE_2T_3X_5$ compounds**

Compounds  $RE_2T_3X_5$  ( $RE$  = rare-earth,  $T$  = transition metal,  $X$  = Si, Ge) with either the  $U_2Co_3Si_5$  or the  $Sc_2Fe_3Si_5$  structure type may or may not develop a CDW. We have found that CDW formation in these compounds can be related to their lattice parameters, according to the value of  $c/\sqrt{ab}$ .

We have compiled a list of 235 materials from the handbook on 2:3:5 materials<sup>20</sup> and other sources,<sup>65–116</sup> along with their values of  $c/\sqrt{ab}$ . Compounds with a monoclinic structure are not included. Also, we do not consider 2:3:5 stannides or gallides, as their lattice parameters are completely different from compounds with the  $U_2Co_3Si_5$  or  $Sc_2Fe_3Si_5$  structure types.<sup>20</sup> Currently, we expect that  $c/\sqrt{ab}$  falls between 0.5260 to 0.5432 for those compounds that undergo CDW and/or structural phase transitions. Basically we consider five scenarios.

Case 1: Confirmed CDW/structural transition and fulfilled criterion.

Case 2: Confirmed CDW/structural transition and outside criterion.

Case 3: Confirmed absence of CDW/structural transition (e.g. by temperature-dependent

physical properties which are published) and fulfilled criterion (i.e. outside the CDW/structural transition range).

Case 4: Confirmed absence of CDW/structural transition and violated criterion.

Case 5: No CDW/structural transition reported, but experiments have not been done that could confirm the presence/absence of a CDW.

A CDW or any other structural transition is likely to proceed at some temperature, if the  $c/\sqrt{ab}$  lies in the range:  $0.5260 < c/\sqrt{ab} < 0.5432$ , while compounds with  $c/\sqrt{ab}$  outside this range do not have a phase transition (Fig. 12). There are three materials that

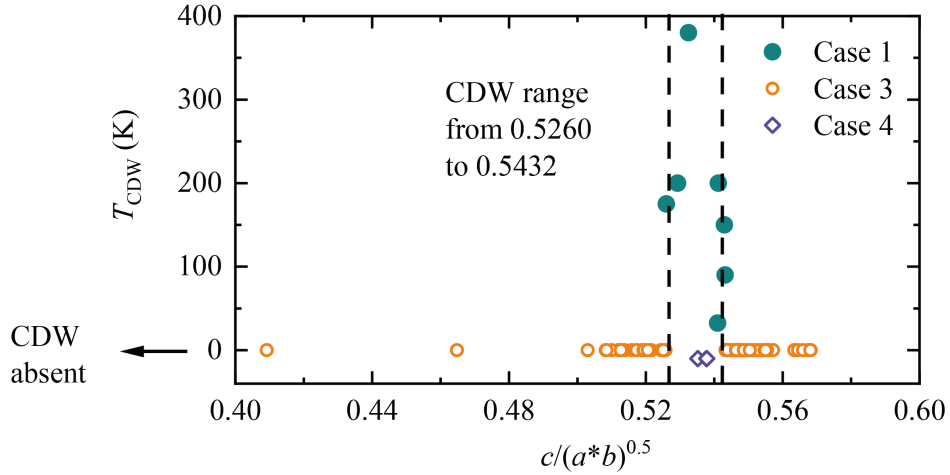


Figure 12: Plot showing  $T_{CDW}$  vs  $c/\sqrt{ab}$  for cases 1, 3 and 4. There are no materials which qualify for case 2.

fulfil the criterion, but do not form a CDW (case 4). They are  $La_2Rh_3Si_5$ ,  $Lu_2Rh_3Si_5$  and  $Yb_2Pd_3Ge_5$ .<sup>72,97</sup> The absence of a phase transition might be related to a large number of defects, as they can be found in polycrystalline materials. Suppression of CDW is known to occur in materials with chemical disorder or defects like vacancies. Examples include  $CuV_2S_4$ ,  $NiV_2Se_4$ ,  $ErTe_3$ .<sup>51,117,118</sup>

Figure 13 collects all materials where there are no structural transitions reported due to lack of evidence from measurements. Many of these compounds that fall within the criterion are the  $RE_2Rh_3Si_5$  series which are reported to exhibit AFM transitions from the physical

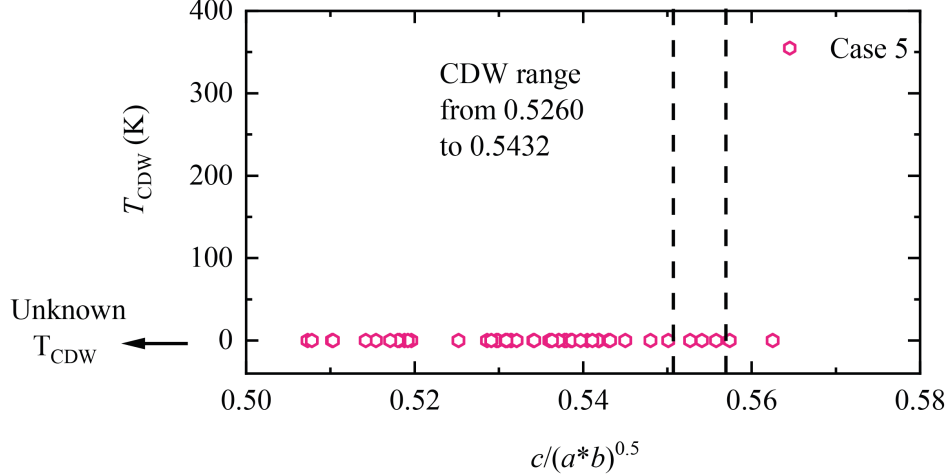


Figure 13: Plot showing  $T_{\text{CDW}}$  vs  $c/\sqrt{ab}$  for case 5.

properties.<sup>97</sup> However, no diffraction experiments have been done to see the AFM is coupled to the lattice to induce a structural distortion. The observed criterion can be used for the prediction of compounds that might form a CDW (Fig. 13). These compounds are listed as case 5 in table S8 in the supporting information. This table provides a complete list of materials used in the discussion.<sup>31</sup>

## Conclusions

We have synthesized a new polymorph of  $\text{Gd}_2\text{Os}_3\text{Si}_5$  and established that it is a high temperature CDW compound. The CDW transition occurs below 400 K according to the SXRD measurements, presumably close to 345 K as indicated by the anomalies detected in the magnetic susceptibility. The CDW crystal structure of the modulated phase indicates that there is a lowering from tetragonal ( $P4/mnc$ ) to orthorhombic symmetry ( $Cccm(\sigma 00)0s0$ ) at the transition. There is no distortion in the lattice away from tetragonal symmetry as the modulation solely causes the reduction in the overall symmetry. The CDW appears to be primarily influenced by the Si2a atoms due to the large modulation displacements of these atoms, also in agreement with  $\text{Sm}_2\text{Ru}_3\text{Ge}_5$ , as the Ge atoms have been reported to possess the largest modulation amplitudes.<sup>7</sup> Electronic structure simulations rule out the Fermi sur-

face nesting and hidden nesting, strong electron correlations, and a large electronic density of states (EDOS) near the Fermi level ( $E_F$ ) having degenerate branches as the possible origin of CDW formations and suggest wave vector-dependent electron-phonon coupling to be the governing mechanism. Lastly, we also reported that CDW in the 2:3:5 systems are influenced by a criterion which is based on the value of  $c/\sqrt{ab}$  being between 0.5260 and 0.5432. This criterion can be useful to predict possible new CDW compounds in the 2:3:5 family.

## Supporting information

The Supporting Information is available free of charge at [URL to be inserted by the publisher].

1. Details of the SXRD data collection, data processing, structural analysis and DFT (PDF).
2. CIF of the periodic and periodic and incommensurately modulated structures at various temperatures.

## Acknowledgement

We thank C. Paulmann for the assistance in collecting SXRD data at Beamline P24. We thank Dr. C. D. Malliakas and Prof. Dr. M. Kanatzidis for providing the SXRD data of the modulated structure of  $\text{Sm}_2\text{Ru}_3\text{Ge}_5$ . We acknowledge DESY (Hamburg, Germany), a member of the Helmholtz Association HGF, for the provision of experimental facilities. Parts of this research were carried out at PETRA III, using beamline P24. Beamtime was allocated for proposal I-20220188.

## References

- (1) Wilson, J. A.; DiSalvo, F. J.; Mahajan, S. Charge-density waves in metallic, layered transition-metal dichalcogenides. *Phys. Rev. Lett.* **1974**, *32*, 882–885.
- (2) Wilson, J. A.; DiSalvo, F. J.; Mahajan, S. Charge-density waves and superlattices in the metallic layered transition metal dichalcogenides. *Adv. Phys.* **1975**, *24*, 117–201.
- (3) Grüner, G. The dynamics of charge-density waves. *Rev. Mod. Phys.* **1988**, *60*, 1129–1181.
- (4) Teng, X.; Chen, L.; Ye, F.; Rosenberg, E.; Liu, Z.; Yin, J.-X.; Jiang, Y.-X.; Oh, J. S.; Hasan, M. Z.; Neubauer, K. J.; others Discovery of charge density wave in a kagome lattice antiferromagnet. *Nature* **2022**, *609*, 490–495.
- (5) Liu, G.; Debnath, B.; Pope, T. R.; Salguero, T. T.; Lake, R. K.; Balandin, A. A. A charge-density-wave oscillator based on an integrated tantalum disulfide–boron nitride–graphene device operating at room temperature. *Nature nanotechnology* **2016**, *11*, 845–850.
- (6) Meier, W. R.; Chakoumakos, B. C.; Okamoto, S.; McGuire, M. A.; Hermann, R. P.; Samolyuk, G. D.; Gao, S.; Zhang, Q.; Stone, M. B.; Christianson, A. D.; others A catastrophic charge density wave in  $\text{BaFe}_2\text{Al}_9$ . *Chemistry of Materials* **2021**, *33*, 2855–2863.
- (7) Bugaris, D. E.; Malliakas, C. D.; Han, F.; Calta, N. P.; Sturza, M.; Krogstad, M. J.; Osborn, R.; Rosenkranz, S.; Ruff, J. P. C.; Trimarchi, G.; Bud’ko, S. L.; Balasubramanian, M.; Chung, D. Y.; Kanatzidis, M. G. Charge Density Wave in the New Polymorphs of  $\text{RE}_2\text{Ru}_3\text{Ge}_5$  (RE= Pr, Sm, Dy). *Journal of the American Chemical Society* **2017**, *139*, 4130–4143.

- (8) Zhao, Y.; Yang, W.; Schnyders, H. S.; Husmann, A.; Zhang, G.; Ren, Y.; Price, D. L.; Mao, H.-K.; Saboungi, M.-L. Pressure-induced charge density wave phase in  $\text{Ag}_{2-\delta}\text{Te}$ . *Physical Review B* **2018**, *98*, 205126.
- (9) Chen, H.; Malliakas, C. D.; Narayan, A.; Fang, L.; Chung, D. Y.; Wagner, L. K.; Kwok, W.-K.; Kanatzidis, M. G. Charge Density Wave and Narrow Energy Gap at Room Temperature in 2D  $\text{Pb}_{3-x}\text{Sb}_{1+x}\text{S}_4\text{Te}_{2-\delta}$  with Square Te Sheets. *Journal of the American Chemical Society* **2017**, *139*, 11271–11276.
- (10) Wandel, S. et al. Enhanced charge density wave coherence in a light-quenched, high-temperature superconductor. *Science* **2022**, *376*, 860–864.
- (11) Li, H. et al. Observation of Unconventional Charge Density Wave without Acoustic Phonon Anomaly in Kagome Superconductors  $\text{AV}_3\text{Sb}_5$  ( $A = \text{Rb}, \text{Cs}$ ). *Phys. Rev. X* **2021**, *11*, 031050.
- (12) Gao, W.; Addiego, C.; Wang, H.; Yan, X.; Hou, Y.; Ji, D.; Heikes, C.; Zhang, Y.; Li, L.; Huyan, H.; others Real-space charge-density imaging with sub-ångström resolution by four-dimensional electron microscopy. *Nature* **2019**, *575*, 480–484.
- (13) Meyer, J. C.; Kurasch, S.; Park, H. J.; Skakalova, V.; Künzel, D.; Groß, A.; Chuvilin, A.; Algara-Siller, G.; Roth, S.; Iwasaki, T.; Starke, U.; Smet, J. H.; Ute Kaiser, U. Experimental analysis of charge redistribution due to chemical bonding by high-resolution transmission electron microscopy. *Nature materials* **2011**, *10*, 209–215.
- (14) Wu, T.; Mayaffre, H.; Krämer, S.; Horvatić, M.; Berthier, C.; Hardy, W.; Liang, R.; Bonn, D.; Julien, M.-H. Magnetic-field-induced charge-stripe order in the high-temperature superconductor  $\text{YBa}_2\text{Cu}_3\text{O}_y$ . *Nature* **2011**, *477*, 191–194.
- (15) Loret, B.; Auvray, N.; Gallais, Y.; Cazayous, M.; Forget, A.; Colson, D.; Julien, M.-H.;

- Paul, I.; Civelli, M.; Sacuto, A. Intimate link between charge density wave, pseudogap and superconducting energy scales in cuprates. *Nature Physics* **2019**, *15*, 771–775.
- (16) Chen, R. Y.; Zhang, S. J.; Zhang, M. Y.; Dong, T.; Wang, N. L. Revealing Extremely Low Energy Amplitude Modes in the Charge-Density-Wave Compound LaAgSb<sub>2</sub>. *Phys. Rev. Lett.* **2017**, *118*, 107402.
- (17) Ramakrishnan, S. et al. Coupling between Charge Density Wave Ordering and Magnetism in Ho<sub>2</sub>Ir<sub>3</sub>Si<sub>5</sub>. *Chem. Mater.* **2023**, *35*, 1980–1990.
- (18) Ramakrishnan, S.; Schönleber, A.; Rekiş, T.; van Well, N.; Noohinejad, L.; van Smaalen, S.; Tolkiehn, M.; Paulmann, C.; Bag, B.; Thamizhavel, A.; Pal, D.; Ramakrishnan, S. Unusual charge density wave transition and absence of magnetic ordering in Er<sub>2</sub>Ir<sub>3</sub>Si<sub>5</sub>. *Phys. Rev. B* **2020**, *101*, 060101(R).
- (19) Ramakrishnan, S.; Schönleber, A.; Bao, J.-K.; Rekiş, T.; Kotla, S. R.; Schaller, A. M.; van Smaalen, S.; Noohinejad, L.; Tolkiehn, M.; Paulmann, C.; Sangeetha, N. S.; Pal, D.; Thamizhavel, A.; Ramakrishnan, S. Modulated crystal structure of the atypical charge density wave state of single-crystal Lu<sub>2</sub>Ir<sub>3</sub>Si<sub>5</sub>. *Phys. Rev. B* **2021**, *104*, 054116.
- (20) Brown, W. K.; Plata, M. A.; Raines, M. E.; Chan, J. Y. *Handbook on the Physics and Chemistry of Rare Earths*; Elsevier, 2023.
- (21) Kuo, C. N.; Hsu, C. J.; Tseng, C. W.; Chen, W. T.; Lin, S. Y.; Liu, W. Z.; Kuo, Y. K.; Lue, C. S. Charge density wave like behavior with magnetic ordering in orthorhombic Sm<sub>2</sub>Ru<sub>3</sub>Ge<sub>5</sub>. *Phys. Rev. B* **2020**, *101*, 155140.
- (22) Sokkalingam, R.; Lingannan, G.; Sundaramoorthy, M.; Lue, C. S.; Kuo, C. N.; Joseph, B.; Arumugam, S. Evidence of structural modulations induced by a charge density wave transition in orthorhombic Sm<sub>2</sub>Ru<sub>3</sub>Ge<sub>5</sub>. *Solid State Communications* **2023**, *372*, 115293.



- (23) Singh, Y.; Pal, D.; Ramakrishnan, S. Low-temperature studies of the magnetic and superconducting properties of the  $R_2\text{Ir}_3\text{Si}_5$  ( $R = \text{Y, La, Ce-Nd, Gd-Tm}$ ) system. *Phys. Rev. B* **2004**, *70*, 064403.
- (24) Sanki, S.; Sharma, V.; Sasmal, S.; Saini, V.; Dwari, G.; Maity, B. B.; Kulkarni, R.; Prakash Pandeya, R.; Mondal, R.; Lakshan, A.; Ramakrishnan, S.; Pratim Jana, P.; Maiti, K.; Thamizhavel, A. Valence fluctuation in  $\text{Ce}_2\text{Re}_3\text{Si}_5$  and Ising-type magnetic ordering in  $\text{Pr}_2\text{Re}_3\text{Si}_5$  single crystals. *Phys. Rev. B* **2022**, *105*, 165134.
- (25) Sharma, V.; Dan, S.; Nandi, S.; Dwari, G.; Maity, B. B.; Sanki, S.; Kulkarni, R.; Thamizhavel, A. Complex magnetic behavior in  $\text{Ho}_2\text{Re}_3\text{Si}_5$  single crystal. *Phys. Rev. Mater.* **2022**, *6*, 124406.
- (26) Mykhalichko, V.; Demchenko, P.; Gladyshevskii, R. NEW TERNARY SILICIDES OF GADOLINIUM AND OSMIUM/PLATINUM. *Bulletin of Lviv University. Series of chemicals* **2015**, *1*, 93–101.
- (27) Parsons, S. Introduction to twinning. *Acta Crystallographica Section D* **2003**, *59*, 1995–2003.
- (28) Fu, W.; Qiao, J.; Zhao, X.; Chen, Y.; Fu, D.; Yu, W.; Leng, K.; Song, P.; Chen, Z.; Yu, T.; others Room temperature commensurate charge density wave on epitaxially grown bilayer 2H-tantalum sulfide on hexagonal boron nitride. *ACS nano* **2020**, *14*, 3917–3926.
- (29) Fragkos, S.; Sant, R.; Alvarez, C.; Bosak, A.; Tsipas, P.; Tsoutsou, D.; Okuno, H.; Renaud, G.; Dimoulas, A. Room temperature commensurate charge density wave in epitaxial strained  $\text{TiTe}_2$  multilayer films. *Advanced Materials Interfaces* **2019**, *6*, 1801850.
- (30) Feng, J.; Susilo, R. A.; Lin, B.; Deng, W.; Wang, Y.; Li, B.; Jiang, K.; Chen, Z.; Xing, X.; Shi, Z.; others Achieving Room-Temperature Charge Density Wave in

Transition Metal Dichalcogenide  $1T$ -VSe<sub>2</sub>. *Advanced Electronic Materials* **2020**, *6*, 1901427.

- (31) See Supplemental Material at [URL will be inserted by publisher] for details on the diffraction experiments and values of the structural parameters, including the citation **add any cites here**.
- (32) Rodriguez-Carvajal, J. *Physica B* **1993**, *95*, 192–202.
- (33) Schreurs, A. M. M.; Xian, X.; Kroon-Batenburg, L. M. J. EVAL15: a diffraction data integration method based on ab initio predicted profiles. *J. Appl. Crystallogr.* **2010**, *43*, 70–82.
- (34) Sheldrick, G. M. *SADABS, Version 2008/1*; Göttingen: University of Göttingen, 2008.
- (35) van Smaalen, S. *Incommensurate Crystallography*; International Union of Crystallography Monographs on Crystallography; OUP Oxford, 2007.
- (36) Wagner, T.; Schönleber, A. A non-mathematical introduction to the superspace description of modulated structures. *Acta Crystallographica Section B* **2009**, *65*, 249–268.
- (37) Stokes, H. T.; Campbell, B. J.; van Smaalen, S. Generation of  $(3 + d)$ -dimensional superspace groups for describing the symmetry of modulated crystalline structures. *Acta Crystallogr. A* **2011**, *67*, 45–55.
- (38) Petricek, V.; Eigner, V.; Dusek, M.; Cejchan, A. Discontinuous modulation functions and their application for analysis of modulated structures with the computing system JANA2006. *Z. Kristallogr.* **2016**, *231*, 301–312.
- (39) Petricek, V.; Dusek, M.; Palatinus, L. Crystallographic computing system JANA2006: general features. *Z. Kristallogr.* **2014**, *229*, 345–352.

- (40) Kresse, G.; Furthmüller, J. Efficiency of ab-initio total energy calculations for metals and semiconductors using a plane-wave basis set. *Computational Materials Science* **1996**, *6*, 15.
- (41) Perdew, J.; Burke, K.; Ernzerhof, M. Generalized gradient approximation made simple. *Physical Review Letters* **1996**, *77*, 3865–3868.
- (42) Dudarev, S.; Botton, G.; Savrasov, S.; Humphreys, C.; Sutton, A. Electron-energy-loss spectra and the structural stability of nickel oxide: An LSDA+U study. *Physical Review B* **1998**, *57*, 1505.
- (43) Hou, Y.; Xiang, H.; Gong, X. Lattice-distortion Induced Magnetic Transition from Low-temperature Antiferromagnetism to High-temperature Ferrimagnetism in Double Perovskites  $A_2FeOsO_6$  ( $A = Ca, Sr$ ). *Scientific Reports* **2015**, *5*, 13159.
- (44) Pizzi, G.; Vitale, V.; Arita, R.; Blügel, S.; Freimuth, F.; Géranton, G.; Gibertini, M.; Gresch, D.; Johnson, C.; Koretsune, T.; others Wannier90 as a community code: new features and applications. *Journal of Physics: Condensed Matter* **2020**, *32*, 165902.
- (45) Dressel, M.; Gruner, G. *Electrodynamics of Solids: Optical Properties of Electrons in Matter*; Cambridge University Press, 2002.
- (46) Johannes, M. D.; Mazin, I. I. Fermi surface nesting and the origin of charge density waves in metals. *Physical Review B* **2008**, *77*, 165135.
- (47) Zhu, X.; Cao, Y.; Zhang, J.; Plummer, E.; Guo, J. Classification of charge density waves based on their nature. *Proceedings of the National Academy of Sciences* **2015**, *112*, 2367–2371.
- (48) Roy, A. P.; Bajaj, N.; Mittal, R.; Babu, P. D.; Bansal, D. Quasi-One-Dimensional Fermi Surface Nesting and Hidden Nesting Enable Multiple Kohn Anomalies in  $\alpha$ -Uranium. *Physical Review Letters* **2021**, *126*, 096401.

- (49) Pathak, A.; Gupta, M. K.; Mittal, R.; Bansal, D. Orbital-and atom-dependent linear dispersion across the Fermi level induces charge density wave instability in  $\text{EuTe}_4$ . *Physical Review B* **2022**, *105*, 035120.
- (50) Pouget, J.-P.; Canadell, E. Structural approach to charge density waves in low-dimensional systems: electronic instability and chemical bonding. *Rep. Prog. Phys.* **2024**, *87*, 026501.
- (51) Ramakrishnan, S.; Schönleber, A.; Hübschle, C. B.; Eisele, C.; Schaller, A. M.; Rekis, T.; Bui, N. H. A.; Feulner, F.; van Smaalen, S.; Bag, B.; Ramakrishnan, S.; Tolkehn, M.; Paulmann, C. Charge density wave and lock-in transitions of  $\text{CuV}_2\text{S}_4$ . *Phys. Rev. B* **2019**, *99*, 195140.
- (52) Ramakrishnan, S. et al. Orthorhombic charge density wave on the tetragonal lattice of  $\text{EuAl}_4$ . *IUCrJ* **2022**, *9*, 378–385.
- (53) Ramakrishnan, S. et al. Noncentrosymmetric, transverse structural modulation in  $\text{SrAl}_4$ , and elucidation of its origin in the  $\text{BaAl}_4$  family of compounds. *Phys. Rev. Res.* **2024**, *6*, 023277.
- (54) Grüner, G. *Density Waves in Solids*; Addison-Wesley: Reading, Massachusetts, 1994.
- (55) Zhu, X.; Guo, J.; Zhang, J.; Plummer, E. Misconceptions associated with the origin of charge density waves. *Advances in Physics: X* **2017**, *2*, 622–640.
- (56) Whangbo, M.-H.; Canadell, E.; Foury, P.; Pouget, J.-P. Hidden Fermi surface nesting and charge density wave instability in low-dimensional metals. *Science* **1991**, *252*, 96–98.
- (57) Weber, F.; Rosenkranz, S.; Castellan, J.-P.; Osborn, R.; Hott, R.; Heid, R.; Bohnen, K.-P.; Egami, T.; Said, A.; Reznik, D. Extended Phonon Collapse and the

- Origin of the Charge-Density Wave in 2H-NbSe<sub>2</sub>. *Physical Review Letters* **2011**, *107*, 107403.
- (58) Weber, F.; Hott, R.; Heid, R.; Bohnen, K.-P.; Rosenkranz, S.; Castellán, J.-P.; Osborn, R.; Said, A.; Leu, B.; Reznik, D. Optical phonons and the soft mode in 2H-NbSe<sub>2</sub>. *Physical Review B* **2013**, *87*, 245111.
- (59) Maschek, M.; Rosenkranz, S.; Heid, R.; Said, A.; Giraldo-Gallo, P.; Fisher, I.; Weber, F. Wave-vector-dependent electron-phonon coupling and the charge-density-wave transition in TbTe<sub>3</sub>. *Physical Review B* **2015**, *91*, 235146.
- (60) Maschek, M.; Zocco, D.; Rosenkranz, S.; Heid, R.; Said, A.; Alatas, A.; Walmsley, P.; Fisher, I.; Weber, F. Competing soft phonon modes at the charge-density-wave transitions in DyTe<sub>3</sub>. *Physical Review B* **2018**, *98*, 094304.
- (61) Chen, C.-W.; Choe, J.; Morosan, E. Charge density waves in strongly correlated electron systems. *Reports on Progress in Physics* **2016**, *79*, 084505.
- (62) Gerber, S.; Jang, H.; Nojiri, H.; Matsuzawa, S.; Yasumura, H.; Bonn, D.; Liang, R.; Hardy, W.; Islam, Z.; Mehta, A.; others Three-dimensional charge density wave order in YBa<sub>2</sub>Cu<sub>3</sub>O<sub>6.67</sub> at high magnetic fields. *Science* **2015**, *350*, 949–952.
- (63) Boring, A.; Smith, J. Plutonium condensed-matter physics: a survey of theory and experiment. *Los Alamos Science* **2000**, *26*, 90–127.
- (64) Söderlind, P.; Landa, A.; Sadigh, B. Density-functional theory for plutonium. *Advances in Physics* **2019**, *68*, 1–47.
- (65) Kyrk, T. M.; Kennedy, E. R.; Galeano-Cabral, J.; Wei, K.; McCandless, G. T.; Scott, M. C.; Baumbach, R. E.; Chan, J. Y. Anisotropic magnetic and transport properties of orthorhombic o-Pr<sub>2</sub>Co<sub>3</sub>Ge<sub>5</sub>. *Journal of Physics: Materials* **2022**, *5*, 044007.

- (66) Godart, C.; Tomy, C.; Gupta, L.; Vijayaraghavan, R. Moment instabilities and magnetic ordering in  $\text{Ce}_2\text{Rh}_3\text{Ge}_5$  and  $\text{Ce}_2\text{Ir}_3\text{Ge}_5$ . *Solid State Communications* **1988**, *67*, 677–680.
- (67) Anand, V.; Nandy, A.; Dhar, S.; Geibel, C.; Hossain, Z. Magnetic and transport properties of  $\text{Pr}_2\text{Ni}_3\text{Ge}_5$ . *Journal of Magnetism and Magnetic Materials* **2007**, *313*, 164–167.
- (68) Nakamura, A.; Okazaki, T.; Nakashima, M.; Amako, Y.; Matsubayashi, K.; Uwatoko, Y.; Kayama, S.; Kagayama, T.; Shimizu, K.; Uejo, T.; Akamine, H.; Hedo, M.; Nakama, T.; Ōnuki, Y.; Shiba, H. Pressure-Induced Valence Transition and Heavy Fermion State in  $\text{Eu}_2\text{Ni}_3\text{Ge}_5$  and  $\text{EuRhSi}_3$ . *Journal of the Physical Society of Japan* **2015**, *84*, 053701.
- (69) Freccero, R.; De Negri, S.; Rogl, G.; Binder, G.; Michor, H.; Rogl, P. F.; Saccone, A.; Solokha, P.  $\text{La}_2\text{Pd}_3\text{Ge}_5$  and  $\text{Nd}_2\text{Pd}_3\text{Ge}_5$  Compounds: Chemical Bonding and Physical Properties. *Inorganic Chemistry* **2021**, *60*, 3345–3354.
- (70) Anand, V. K.; Hossain, Z.; Geibel, C. Magnetic order in  $\text{Pr}_2\text{Pd}_3\text{Ge}_5$  and possible heavy-fermion behavior in  $\text{Pr}_2\text{Rh}_3\text{Ge}_5$ . *Phys. Rev. B* **2008**, *77*, 184407.
- (71) Kurenbaeva, J.; Seropegin, Y.; Bodak, O.; Nikiforov, V. Investigation of the interactions of the components in the Sm-Pd-Ge system. *Journal of Alloys and Compounds* **1998**, *269*, 151–156.
- (72) Freccero, R.; Choi, S.; Solokha, P.; De Negri, S.; Takeuchi, T.; Hirai, S.; Mele, P.; Saccone, A. Synthesis, crystal structure and physical properties of  $\text{Yb}_2\text{Pd}_3\text{Ge}_5$ . *Journal of Alloys and Compounds* **2019**, *783*, 601–607.
- (73) Becker, B.; Ramakrishnan, S.; Groten, D.; Süllow, S.; Mattheus, C.; Nieuwenhuys, G.; Mydosh, J. Magnetic behaviour of the new intermetallic compound  $\text{Ce}_2\text{Pd}_3\text{Ge}_5$ . *Physica B: Condensed Matter* **1997**, *230-232*, 253–255.

- (74) Hossain, Z.; Hamashima, S.; Umeo, K.; Takabatake, T.; Geibel, C.; Steglich, F. Antiferromagnetic transitions in the Kondo lattice system  $\text{Ce}_2\text{Ni}_3\text{Ge}_5$ . *Phys. Rev. B* **2000**, *62*, 8950–8953.
- (75) Gamza, M. B.; Gumeniuk, R.; Burkhardt, U.; Schnelle, W.; Rosner, H.; Leithe-Jasper, A.; Slebarski, A. Coexistence of magnetic order and valence fluctuations in the Kondo lattice system  $\text{Ce}_2\text{Rh}_3\text{Sn}_5$ . *Phys. Rev. B* **2017**, *95*, 165142.
- (76) Li, D. X.; Honda, F.; Miyake, A.; Homma, Y.; Haga, Y.; Nakamura, A.; Shimizu, Y.; Maurya, A.; Sato, Y. J.; Tokunaga, M.; Aoki, D. Magnetic and electrical properties of the ternary compound  $\text{U}_2\text{Ir}_3\text{Si}_5$  with one-dimensional uranium zigzag chains. *Phys. Rev. B* **2019**, *99*.
- (77) Bugaris, D. E.; Malliakas, C. D.; Bud'ko, S. L.; Calta, N. P.; Chung, D. Y.; Kanatzidis, M. G. Flux Crystal Growth of the  $\text{RE}_2\text{Ru}_3\text{Ge}_5$  (RE = La, Ce, Nd, Gd, Tb) Series and Their Magnetic and Metamagnetic Transitions. *Inorganic Chemistry* **2017**, *56*, 14584–14595.
- (78) Mazumdar, C.; Nagarajan, R.; Dhar, S. K.; Gupta, L. C.; Vijayaraghavan, R.; Padalia, B. D.  $\text{Ce}_2\text{Ni}_3\text{Si}_5$ : A mixed-valence cerium compound. *Phys. Rev. B* **1992**, *46*, 9009–9012.
- (79) Kamadurai, R. K.; Fobasso, R. D.; Maurya, A.; Ramankutty, P. K.; Strydom, A. M. Ferromagnetic Ordering and Heavy Fermion Behaviour in  $\text{Ce}_2\text{Ru}_3\text{Ge}_5$ . *Journal of the Physical Society of Japan* **2020**, *89*, 064705.
- (80) Mazumdar, C.; Nigam, A. K.; Nagarajan, R.; Gupta, L. C.; Chandra, G.; Padalia, B. D.; Godart, C.; Vijayaraghavan, R. Anomalous magnetoresistance in antiferromagnetic polycrystalline materials  $\text{R}_2\text{Ni}_3\text{Si}_5$  (R=rare earth). *Journal of Applied Physics* **1997**, *81*, 5781–5783.

- (81) Mazumdar, C.; Nagarajan, R.; Nigam, A. K.; Ghosh, K.; Ramakrishnan, S.; Gupta, L. C.; Padalia, B. D. Double magnetic transition and anomalous magnetoresistance in  $\text{Er}_2\text{Ni}_3\text{Si}_5$ . *Physica B: Condensed Matter* **2003**, *339*, 216–220.
- (82) Mazumdar, C.; Ghosh, K.; Nagarajan, R.; Ramakrishnan, S.; Padalia, B. D.; Gupta, L. C. Low-temperature heat-capacity studies of  $R_2\text{Ni}_3\text{Si}_5$  ( $R = \text{Pr, Nd, Sm, Gd, Tb, Dy, Ho}$ ). *Phys. Rev. B* **1999**, *59*, 4215–4220.
- (83) Hashimoto, Y.; Kawano, S.; Koyano, N.; Takahashi, M. Neutron and X-ray diffraction studies on the  $\text{Tb}_2\text{Ni}_3\text{Si}_5$  single crystal. *Journal of Physics and Chemistry of Solids* **2007**, *68*, 2095–2098.
- (84) Mazumdar, C.; Nagarajan, R.; Gupta, L. C.; Vijayaraghavan, R.; Godart, C.; Padalia, B. D. Magnetic properties of two new compounds:  $\text{Gd}_2\text{Ni}_3\text{Si}_5$  and  $\text{Sm}_2\text{Ni}_3\text{Si}_5$ . *Journal of Applied Physics* **1994**, *75*, 7155–7157.
- (85) Huo, D.; Sakurai, J.; Kuwai, T.; Mizushima, T.; Isikawa, Y. Antiferromagnetism in the Kondo lattice compound  $\text{Ce}_2\text{Pd}_3\text{Si}_5$ . *Phys. Rev. B* **2002**, *65*, 144450.
- (86) Muro, Y.; Nakano, M.; Motoya, K. Single-crystal study of new Ce compound  $\text{Ce}_2\text{Pt}_3\text{Si}_5$ . *Physica B: Condensed Matter* **2008**, *403*, 810–811.
- (87) Anand, V.; Anupam; Hossain, Z.; Ramakrishnan, S.; Thamizhavel, A.; Adroja, D. Magnetic and transport properties of  $\text{Pr}_2\text{Pt}_3\text{Si}_5$ . *Journal of Magnetism and Magnetic Materials* **2012**, *324*, 2483–2487.
- (88) Kurenbaeva, J.; Seropegin, Y.; Griбанov, A.; Bodak, O.; Nikiforov, V. Crystal structure of compounds with 20% Sm in the Sm-Pd, Pt-Si,Ge systems at 870 K. *Journal of Alloys and Compounds* **1999**, *285*, 137–142.
- (89) Nirmala, R.; Sankaranarayanan, V.; Sethupathi, K. Reentrant ferromagnetism in  $\text{Gd}_2\text{Mn}_3\text{Ge}_5$ . *Physica B: Condensed Matter* **2000**, *284-288*, 1337–1338.



- (90) Griveau, J.-C.; Colineau, E.; Bouëxiere, D.; Gofryk, K.; Klimczuk, T.; Rebizant, J. Magnetic properties of ferromagnetic  $\text{Pu}_2\text{Pt}_3\text{Si}_5$ . *Journal of Alloys and Compounds* **2013**, *576*, 409–414.
- (91) Sarkar, S.; Subbarao, U.; Joseph, B.; Peter, S. C. Mixed valence and metamagnetism in a metal flux grown compound  $\text{Eu}_2\text{Pt}_3\text{Si}_5$ . *Journal of Solid State Chemistry* **2015**, *225*, 181–186.
- (92) Bauer, E. D.; Tobash, P. H.; Mitchell, J. N.; Kennison, J. A.; Ronning, F.; Scott, B. L.; Thompson, J. D. Magnetic order in  $\text{Pu}_2\text{M}_3\text{Si}_5$  ( $M = \text{Co}, \text{Ni}$ ). *Journal of Physics: Condensed Matter* **2011**, *23*, 094223.
- (93) Skanthakumar, S.; Lynn, J. W.; Mazumdar, C.; Nagarajan, R.; Gupta, L. C. Magnetic phase transitions in  $R_2\text{Ni}_3\text{Si}_5$ . *Physica B: Condensed Matter* **1997**, *241-243*, 693–695.
- (94) Mazumdar, C.; Nigam, A. K.; Nagarajan, R.; Gupta, L. C.; Godart, C.; Padalia, B. D.; Chandra, G.; Vijayaraghavan, R. Anomalous magnetoresistance behavior of  $R_2\text{Ni}_3\text{Si}_5$  ( $R = \text{Pr}, \text{Dy}, \text{Ho}$ ). *Phys. Rev. B* **1996**, *54*, 6069–6072.
- (95) Singh, Y.; Pal, D.; Ramakrishnan, S. Low-temperature studies of the magnetic and superconducting properties of the  $R_2\text{Ir}_3\text{Si}_5$  ( $R = \text{Y}, \text{La}, \text{Ce-Nd}, \text{Gd-Tm}$ ) system. *Phys. Rev. B* **2004**, *70*, 064403.
- (96) Patil, N.; Ramakrishnan, S. Study of magnetism in  $R_2\text{Rh}_3\text{Si}_5$  ( $R = \text{Gd}, \text{Tb}, \text{Dy}, \text{Ho}, \text{Er}, \text{Tm}$ ) system. *Physica B: Condensed Matter* **1997**, *237-238*, 597–598.
- (97) Ramakrishnan, S.; Patil, N. G.; Chinchure, A. D.; Marathe, V. R. Magnetism and crystal-field effects in the  $R_2\text{Rh}_3\text{Si}_5$  ( $R = \text{La}, \text{Ce}, \text{Pr}, \text{Nd}, \text{Tb}, \text{Gd}, \text{Dy}, \text{Er}, \text{Ho}, \text{and Tm}$ ) system. *Phys. Rev. B* **2001**, *64*, 064514.
- (98) Paccard, D.; Paccard, L.  $\text{Y}_2\text{Rh}_3\text{Si}_5$ ,  $\text{Dy}_2\text{Rh}_3\text{Si}_5$  with a monoclinic structural deforma-

- tion variant of the orthorhombic  $U_2Co_3Si_5$ -type structure. *Journal of the Less Common Metals* **1987**, *128*, 125–129.
- (99) Chevalier, B.; Lejay, P.; Etourneau, J.; Vlasse, M.; Hagenmuller, P. Structure, superconductivity and magnetism of new rare earth-rhodium silicides  $RE_2Rh_3Si_5$  of  $U_2Co_3Si_5$ -type. *Materials Research Bulletin* **1982**, *17*, 1211–1220.
- (100) Paccard, D.; Paccard, L.  $R_2Ru_3Si_5$  ( $R = Er, Tb$ ) with the orthorhombic  $U_2Co_3Si_5$ -type structure and  $R_2Ru_3Si_{4.6}$  ( $R = Gd, Tb, Dy, Ho, Er$ ) and  $R_2Os_3Si_{4.6}$  ( $R = Tb, Er$ ) with the tetragonal  $Sc_2Fe_3Si_5$ -type structure. *Journal of the Less Common Metals* **1990**, *163*, L13–L17.
- (101) Griбанov, A.; Grytsiv, A.; Rogl, P.; Seropegin, Y.; Giester, G. X-ray structural study of intermetallic alloys  $RT_2Si$  and  $RTSi_2$  ( $R$ =rare earth,  $T$ =noble metal). *Journal of Solid State Chemistry* **2010**, *183*, 1278–1289.
- (102) Rizzoli, C.; Salamakha, P.; Sologub, O.; Belletti, D.; Gonçalves, A.; Almeida, M. X-Ray single-crystal investigation of rare earth osmium silicides. *Journal of Alloys and Compounds* **2004**, *363*, 222–227.
- (103) Singh, Y.; Ramakrishnan, S.; Hossain, Z.; Geibel, C. Antiferromagnetic ordering in the Kondo lattice system  $Yb_2Fe_3Si_5$ . *Phys. Rev. B* **2002**, *66*, 014415.
- (104) Watanabe, T.; Sasame, H.; Okuyama, H.; Takase, K.; Takano, Y. Disorder-sensitive superconductivity in the doped iron silicide superconductor  $(Lu_{1-x}R_x)_2Fe_3Si_5$  ( $R=Sc, Y, \text{ and } Dy$ ). *Phys. Rev. B* **2009**, *80*, 100502.
- (105) Vining, C. B.; Shelton, R. N. Low-temperature heat capacity of antiferromagnetic ternary rare-earth iron silicides  $M_2Fe_3Si_5$ . *Phys. Rev. B* **1983**, *28*, 2732–2742.
- (106) Braun, H.; Segre, C.; Acker, F.; Rosenberg, M.; Dey, S.; Deppe, P. Susceptibility and

- Mössbauer studies of magnetic rare earth-iron-silicides. *Journal of Magnetism and Magnetic Materials* **1981**, *25*, 117–123.
- (107) Segre, C.; Braun, H. Reentrant superconductivity in  $\text{Tm}_2\text{Fe}_3\text{Si}_5$ . *Physics Letters A* **1981**, *85*, 372–374.
- (108) Leithe-Jasper, A.; Rogl, P.; Potter, P. Ternary silicides  $\text{Pu}_2\text{T}_3\text{Si}_5$ ,  $\text{T} = \text{Fe}, \text{Tc}, \text{Re}$ . *Journal of Nuclear Materials* **1996**, *230*, 302–305.
- (109) Wastin, F.; Rebizant, J.; Sanchez, J.; Blaise, A.; Goffart, J.; Spirlet, J.; Walker, C.; Fuger, J. New actinide ternary intermetallic compounds: synthesis, characterization and physical properties. *Journal of Alloys and Compounds* **1994**, *210*, 83–89.
- (110) Morozkin, A. V.; Seropegin, Y. D.; Sviridov, I. A. New ternary compounds  $R_2\text{Mn}_3\text{Si}_5$  ( $R=\text{Tb-Er}$ ) with  $\text{Sc}_2\text{Fe}_3\text{Si}_5$ -type structure. *Journal of Alloys and Compounds* **1998**, *270*, L13–L15.
- (111) Morozkin, A.; Seropegin, Y.; Sviridov, I.; Moskalev, V.; Tskhadadze, I.; Ryabinkin, I. Phase equilibria in the  $\{\text{Sm}, \text{Tb}, \text{Tm}\}$ -Mn-Si systems at 870/1070 K: Structural data and melting temperatures of some ternary compounds in the R-Mn-Si systems ( $R=\text{Y}, \text{La-Lu}$ ). *Journal of Alloys and Compounds* **1998**, *280*, 178–187.
- (112) Nirmala, R.; Sankaranarayanan, V.; Morozkin, A.; Sethupathi, K. Multi-magnetic transitions in  $\text{Tb}_2\text{Mn}_3\text{Si}_5$ . *Journal of Alloys and Compounds* **2001**, *316*, L1–L3.
- (113) Nirmala, R.; Sankaranarayanan, V.; Sethupathi, K.; Morozkin, A. Magnetism and electronic transport in  $R_2\text{Mn}_3\text{Si}_5$  ( $R=\text{Dy}, \text{Ho}$  and  $\text{Er}$ ) compounds. *Journal of Alloys and Compounds* **2001**, *325*, 37–41.
- (114) Meot-Meyer, M.; Venturini, G.; Malaman, B.; Mc Rae, E.; Roques, B. Magnetisme et conductivite des siliciures  $\text{Y}_2\text{Mn}_3\text{Si}_5$  et  $\text{Lu}_2\text{Mn}_3\text{Si}_5$ . *Materials Research Bulletin* **1985**, *20*, 1009–1014.

- (115) Chabot, B.; Parthe, E.  $\text{Ce}_2\text{Co}_3\text{Si}_5$  and  $\text{R}_2\text{Ni}_3\text{Si}_5$  ( $\text{R} = \text{Ce}, \text{Dy}, \text{Y}$ ) with the orthorhombic  $\text{U}_2\text{Co}_3\text{Si}_5$ -type structure and the structural relationship with the tetragonal  $\text{Sc}_2\text{Fe}_3\text{Si}_5$ -type structure. *Journal of the Less Common Metals* **1984**, *97*, 285–290.
- (116) Chabot, B.; Parthe, E.  $\text{Dy}_2\text{Co}_3\text{Si}_5$ ,  $\text{Lu}_2\text{Co}_3\text{Si}_5$ ,  $\text{Y}_2\text{Co}_3\text{Si}_5$  and  $\text{Sc}_2\text{Co}_3\text{Si}_5$  with a monoclinic structural deformation variant of the orthorhombic  $\text{U}_2\text{Co}_3\text{Si}_5$  structure type. *Journal of the Less Common Metals* **1985**, *106*, 53–59.
- (117) Ramakrishnan, S.; Matteppanavar, S.; Schönleber, A.; Patra, B.; Singh, B.; Thamizhavel, A.; Singh, B.; Ramakrishnan, S.; van Smaalen, S. Realization of Z2 Topological Metal in Single-Crystalline Nickel Deficient  $\text{NiV}_2\text{Se}_4$ . *Annalen der Physik* **2023**, *535*, 2200611.
- (118) Fang, A.; Straquadine, J. A. W.; Fisher, I. R.; Kivelson, S. A.; Kapitulnik, A. Disorder-induced suppression of charge density wave order: STM study of Pd-intercalated  $\text{ErTe}_3$ . *Phys. Rev. B* **2019**, *100*, 235446.

# TOC Graphic

